Int J Adv Manuf Technol (2017) 90:1393–1417
DOI 10.1007/s00170-016-9429-z

ORIGINAL ARTICLE

Influence of scan strategy and process parameters on microstructure and its optimization in additively manufactured nickel alloy 625 via laser powder bed fusion

Yiğit M. Arısoy[1] · Luis E. Criales[1] · Tuğrul Özel[1] · Brandon Lane[2] · Shawn Moylan[2] · Alkan Donmez[2]

Received: 29 April 2016 / Accepted: 31 August 2016 / Published online: 23 September 2016

Abstract Laser powder bed fusion (L-PBF) as an additive manufacturing process produces nearly fully dense nickel alloy 625 (IN625) parts with complex features. L-PBF generates surfaces and microstructure through directional solidification that can be controlled by scan strategies and selection of process parameters. This study provides experimental investigations on microstructure formation including sizes of cellular grains and growth directions of columnar grains on the nickel alloy 625 test coupons. The effects of process parameters including laser power, scan velocity, hatch distance, and scan strategy that produce various solidification cooling rates and thermal gradients during the process, which also contribute to resultant microstructure, have been analyzed. Optimization studies are conducted on several objectives to improve the productivity while controlling the process effects on the resultant microstructure using response surface regression, desirability functions, and multi-objective genetic algorithm optimization.

✉ Tuğrul Özel
ozel@rutgers.edu

[1] Department of Industrial & Systems Engineering, Rutgers, The State University of New Jersey, 96 Frelinghuysen Road, Piscataway, NJ 08854, USA

[2] National Institute of Standards and Technology, Engineering Laboratory, Gaithersburg, MD, USA

Keywords Additive manufacturing · Selective laser melting · Laser powder bed fusion · Microstructure · Nickel alloy IN625

1 Introduction

Laser-based powder metal additive manufacturing technology especially for difficult-to-cut materials such as stainless steel (316L), titanium (Ti-6Al-4V), and nickel-based (IN718 or IN625) alloys has been steadily growing and finding applications in various industries including medical implants and automotive and aerospace parts with complex geometries and structures [12]. However, the as-built part quality and process performance in terms of dimensional accuracy, surface roughness, structural integrity, resultant properties, residual stresses, and related processing times has not been at the desired industry-ready levels, and some challenges in structural integrity still remain [18]. Process understanding with predictive capability for improved dimensional quality, roughness, and integrity of surfaces [3] as well as reduced porosity, residual stresses [16], defects, and overall better productivity is of great interest to current on-going research efforts.

While laser-based powder metal additive processes allow manufacturing of parts with sophisticated features, the parts fabricated often require further operations such as hot isostatic pressing (HIP) to improve structural integrity. The surface integrity and layer characteristics of the processed parts play an important role in the product performance and service life. Microstructures of metal parts obtained are significantly different than parts obtained with other manufacturing processes and require better understanding of process-induced effects to be able to control and optimize the resultant part quality. Therefore, investigation of the microstructure and process parameter optimization is of great importance for the industry.

1.1 Laser powder bed fusion of IN625 alloy

Laser powder bed fusion (L-PBF) process is a metal additive manufacturing method where layers of powdered metal are melted locally at specific locations using a high-power laser beam, and a nearly fully dense part sections are fabricated at each layer after solidification according to active ASTM terminology (ASTM52900–15). L-PBF processes such as Selective Laser Melting™, Direct Metal Laser Sintering™, and LaserCUSING™ in particular are advantageous in obtaining fully dense structures without a need for post-processing. The desired three-dimensional (3D) part geometry is realized where the L-PBF machine builds the solidified structure layer-by-layer using 2D sliced geometry by adding a new powder layer on top of the previously processed and solidified layer. In order to minimize the oxidation, an inert gas such as Argon or Nitrogen is pumped into the chamber and the platform is heated up to a temperature on the order of 80 °C prior to laying and processing of the first powder metal layer. Once the process is completed, the excess powder metal is vacuumed and filtered to be reused.

The laser beam is scanned over the powder surface, often in a hatched stripe pattern, using numerically controlled mirrors until a layer is processed as shown in Fig. 1 where both a graphical representation of the laser scanning of hatches and an actual image captured while solidified stripes are created in the powder metal bed.

The L-PBF process works by melting desired locations of the powder bed on a layer. The area to be processed is first divided into stripes. Each stripe consists of multiple tracks, separated by a hatch distance. Each track is processed with the laser beam at a constant scan velocity. After a track is completed by the movement of laser in one direction, the laser turns off and shifts towards the next unprocessed track where it turns back on and starts moving in the opposite direction of the previous track as shown in Fig. 2.

The size of the molten region in the powder bed, called the meltpool, is determined by the process parameters such as scan velocity (v_s), laser power (P), hatch distance (h), laser spot size (d), and the powder particle size distribution (PSD). Material properties such as thermal conductivity (k), specific heat (C_p), density (ρ), and reflectivity (R), as well as

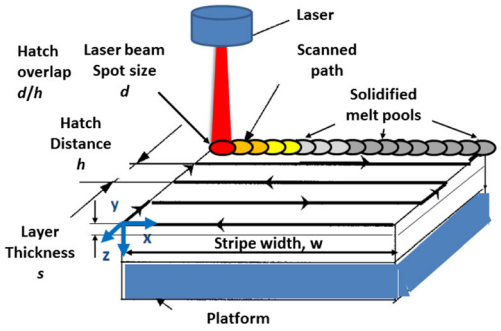

Fig. 2 Definitions of L-PBF terminology [5]

the process environment also have an effect on the meltpool. After a layer is finished, a new layer of powder, with a predefined thickness (s) is placed on the powder bed. For a successful build, it is critical that the meltpool size is large enough to connect the tracks and stripes in each layer and deep enough to connect to the previous layer. Inadequate process parameters can easily cause incomplete fusion which leads to defects in the part and possibly to catastrophic failures during or after the process [10]. Furthermore, process parameters also have a significant effect on the underlying microstructure of the part, which affects the mechanical properties of the material significantly.

It is well known that the geometry and density of the resulting part fabricated with L-PBF will change with the aforementioned process parameters. In the L-PBF process, consecutive layers are built by processing powder material with a given layer thickness [2]. These consecutive layers are processed slightly differently to ensure a robust built. More specifically, stripe orientation changes from layer to layer by a set margin. Two scan strategies that are commonly utilized by L-PBF machines are (a) scan strategy rotation (SSR) = 90° counterclockwise rotation and (b) SSR ≈ 67° counterclockwise rotation between consecutive layers. Figure 3 illustrates this concept for both scan strategy rotations.

This study focuses on the direct effects of process parameters and scan strategy on density and microstructure of the L-PBF processed nickel alloy 625 (IN625) and aims at optimizing some of the parameters to achieve a desirable microstructure. The relations between grain size and growth directions of

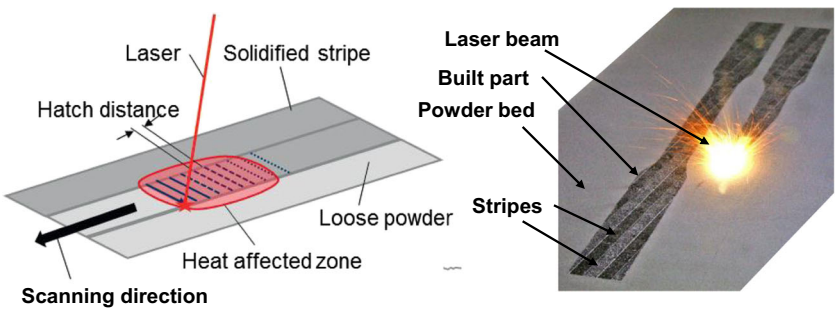

Fig. 1 Laser processing of stripes with hatching in laser powder bed fusion [11]

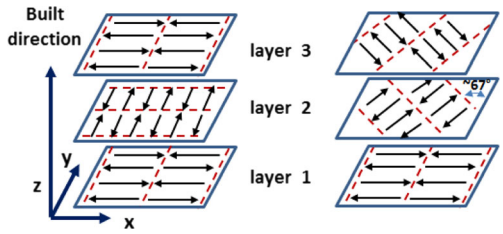

Fig. 3 Schematic of a stripe scan pattern with 90° (*left*) and 67° (*right*) counterclockwise rotations between consecutively built layers [2]

the columnar grains with respect to resultant mechanical strength of the manufactured parts are not studied in this paper. These parts often go through a heat treatment processes, but the alteration to the microstructure and mechanical strength is known to be limited. Therefore, the study first provides experimental investigations on IN625 microstructure including relative density, grain sizes, grain orientations, and growth directions Later, predictive modeling is performed by using experimental design and response surface regression method. Finally, process optimization investigations are conducted by defining tangible process objectives and utilizing multi-objective genetic algorithm (MOGA) type computational methodology with feasible regions of decision variable spaces.

1.2 Microstructure of L-PBF processed nickel alloy IN625

Additive manufacturing of parts made of nickel alloys such as IN625 and IN718 from powder material has been investigated widely. Laser consolidation process yields a microstructure with columnar grains in the build direction [15]. The relative grain size comes from the rapid cooling, and the directionality comes from the thermal gradients during the process. Laser consolidated IN625 maintains the same γ phase as the powder with face-centered cubic (fcc) structure. Moreover, the solidification is observed to be towards the {100} plane of the crystal, which is commonly seen in dendritic growth of fcc grains. The directionality of the microstructure caused anisotropic mechanical behavior with a lower tensile strength in the build direction compared to the horizontal direction [13]. Ramos et al. [20] studied the dendritic-equiaxed transition on the deposited surface in a mask-powder-substrate arrangement and the potential of selective laser melting process for growing single crystal structures in processing nickel-based superalloys.

Wang et al. [24] analyzed the microstructure and mechanical behavior of IN718 alloy parts fabricated using L-PBF. Jia and Gu [9] also analyzed densification, microstructure, and properties of L-PBF-manufactured IN718 parts, establishing a relationship between process parameters and microstructure and mechanical properties. Amato et al. [1] studied microstructure formation in L-PBF of IN718 and investigated formation of γ″ phase precipitate columns within directionally solidified and similarly textured grains. Carter et al. [4] studied the influence of scan strategy on the formation bi-modal grain structure and linked to the overlapping of the "island" pattern in L-PBF fabricated nickel super alloy CM247LC.

In L-PBF processing of nickel-based alloys, the matrix phase γ, with γ′ (primary, secondary, tertiary if exists), γ″, and δ phases as well as dendrite formations can be found in the microstructure, as reported [2, 9, 23]. Coarser cellular structures were also observed in the inter-meltpool regions [2].

Li et al. [14] state that L-PBF process also differs from other laser deposition processes in which a higher heat input is used that causes larger tracks and lower temperature gradients. Rapid solidification during the L-PBF process is said to yield much smaller dendrite arm spaces (around 0.5 μm) compared to traditional casting (100–300 μm). Cellular grains with sizes ranging from 0.2 to 1 μm are observed. The width of the fusion line between meltpool cross-sections is found to be approximately 0.5 μm, and as the temperature outside the fusion line is very high, boundaries of the cellular structures that are primarily composed of Nb are dissolved into the substrate.

During the L-PBF process, the top layer is melted on top of a colder substrate layer, causing a vertical temperature gradient which determines the growth direction. However, rapid convection in various directions during the process causes columnar structures to grow in different directions which are not always aligned towards the vertical axis. Furthermore,

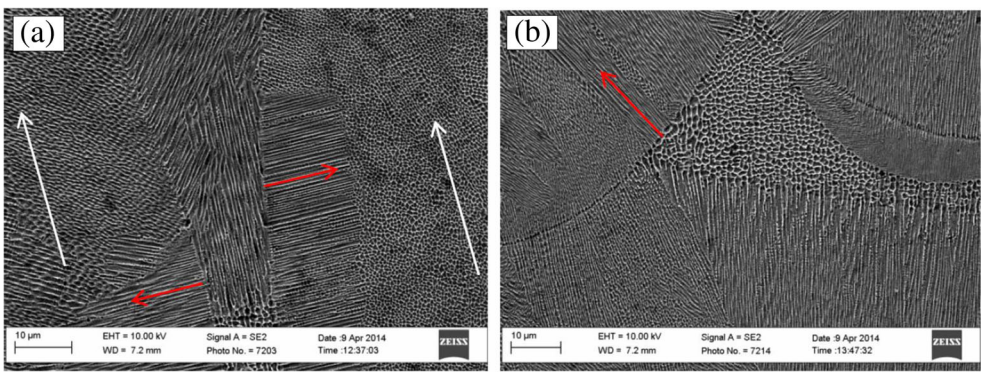

Fig. 4 Microstructure of L-PBF processed IN625 nickel alloy. **a** SEM image of horizontal (XY) section showing cellular/dendritic growth towards the center of the scan track and **b** vertical (YZ) section with dendrites growing towards the track center and in the build direction. Growth direction is marked with *red arrows*, and laser scan track centers are marked with *white arrows* [2]

microstructure of parts obtained from L-PBF is found to be austenitic [23].

Hernandez et al. [7] investigate the microstructure and properties of IN625 alloy after Electron Beam Powder Bed Fusion (EB-PBF) processing. Cellular-like arrays with low-angle grain boundaries are also seen in the horizontal section. Columnar grains of 2 μm spaced γ'' Ni_3Nb body-centered tetragonal (bct) precipitates are observed coinciding with the {111} planes of the NiCr (fcc) γ matrix planes rather than the usual {100} [7, 18, 19].

Hong et al. [8] investigate the laser metal deposition of ultrafine TiC particle reinforced IN625 composite parts and study the effects of laser energy input per unit length on the resultant microstructures. Amato et al. [1] investigate the microstructures on L-PBF and EB-PBF processed IN625 nickel-based alloy parts and effects of hot isostatic pressing. A commercially available L-PBF machine with a 100-μm beam diameter 0.2 kW Yb fiber laser is used to fabricate parts with 800 and 1200 mm/s scan velocities and alternating x/y direction scans.

Microstructure of L-PBF processed IN625 is given in Fig. 4 where dendrites are observed to grow in cells. It is seen in Fig. 4a that the growth direction is towards (or away from) the center of the scan track. Furthermore, in Fig. 4b, meltpools in different layers are observed with dendritic growth occurring towards the track center in the build (Z) direction.

Figure 5 shows a 3D view of L-PBF produced nickel alloy IN100 microstructure in which the build direction is shown by the arrow. Columnar grains are observed in the build direction in the side views. Moreover, cellular grains are also seen in the top (XY) and side views. Cellular grains in the top view have approximately the same diameter as the width of the columnar grains and may in fact be appearing due to cross-sectioning of the columnar grains.

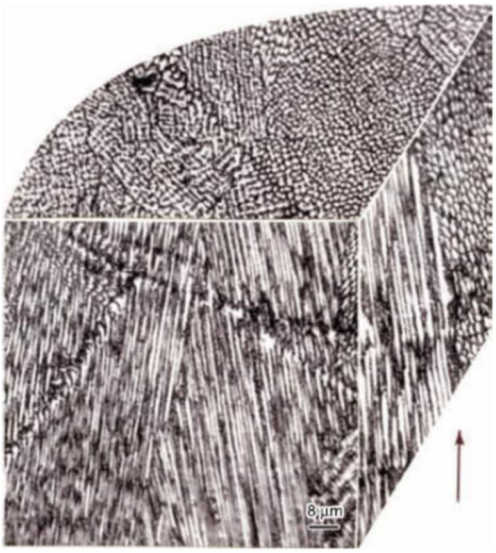

Fig. 5 SEM 3D combined view of L-PBF produced IN100 microstructure [18]

2 Experimental work

The purpose of the experimental work is to develop empirical predictive models describing the relationships between the L-PBF process parameters and the resulting density and microstructure of fabricated parts. A commercial additive manufacturing grade (Micro-Melt 625AM) nickel alloy 625 powder produced by gas atomization process with the average particle size of 35 μm was used. Test coupons in the shape of cubes were manufactured using a commercially available L-PBF machine (EOS M270 Direct Metal Laser Sintering machine) under nitrogen gas ambience at the National Institute for Standards & Technology (NIST) at the National Institute of Standards and Technology. An experimental design suitable for the application of Response Surface Methodology (RSM) was selected. There were two limitations that restricted experimental design selection: (i) a maximum of 36 test coupons could be fabricated due to size constraints in the build platform of the DMLS machine and (ii) hatch distance could only be increased or decreased in intervals of 0.01 mm. The first limitation eliminated the possibility of a three-level factorial design for three factors and two scanning strategies, which would require a minimum of 54 treatments. The second limitation greatly reduced the applicability of Box-Wilson central composite design types, which require high resolution in between levels. Therefore, machine rounding error while input of process settings would have significantly altered the outcome of Box-Wilson type designs. Another alternative, the Box-Behnken design, offered an advantage by requiring comparatively less number of runs while maintaining rotatability. Hence, Box-Behnken design was utilized in the designing of experiments which requires fewer experiments compared to other designs such as full factorial designs, while maintaining rotatability. Furthermore, it allows the analysis of results via RSM for creating predictive models from experimental data.

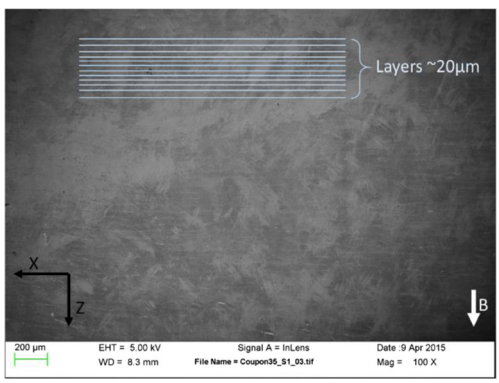

Fig. 6 SEM image of the electropolished XZ surface of the IN625 test coupon, at ×100 magnification. *B* indicates the build direction (P = 195 W, v_s = 800 mm/s, h = 0.10 mm, SSR ≈ 67°)

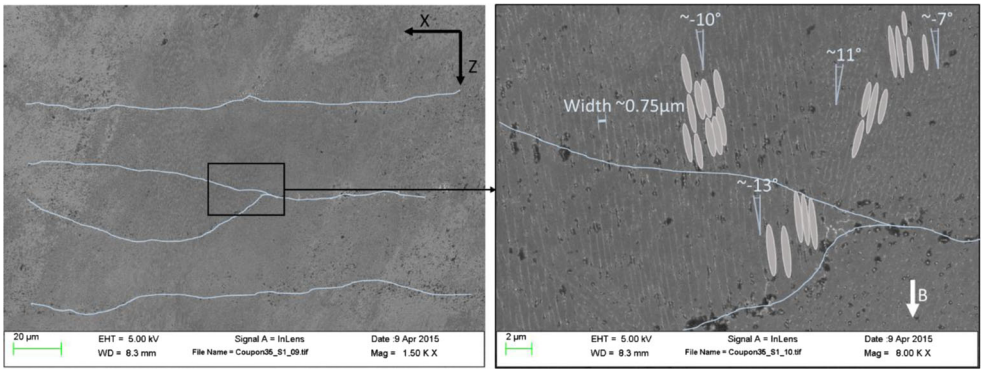

Fig. 7 SEM image of the electropolished XZ surface of the IN625 coupon, at ×1500 magnification (*left*) showing layers and ×8000 magnification (*right*) showing columnar grains with inclinations. *B* indicates the build direction (P = 195 W, v_s = 800 mm/s, h = 0.10 mm, SSR ≈ 67°)

Three process parameters are considered at three levels, namely, laser power (P), scan velocity (v_s), and hatch distance (h). The three-factor Box-Behnken design represents the process space where the treatment combinations appear at the center of the cube as well as on the midpoints of the edges. The three-factor, three-level Box-Behnken design where low, medium, and high settings of each factor are defined as P = 169, 182, and 195 W; v_s = 725, 800, and 875 mm/s; and h = 0.09, 0.10, and 0.11 mm, for power, scan velocity, and hatch distance, respectively. These factors and levels were carefully selected by slightly varying process parameters to assure successful and simultaneous building of 36 cube-shaped parts on the built platform and allowing variations. If any of the 36 cube-shape constructs would fail due to incomplete fusion, the rest of the constructs would be compromised on the same layer and the experiment would have been destroyed.

In addition, energy density is defined as a function of laser power (P), powder layer thickness (s), scan velocity (v_s), and hatch distance (h), as shown in Eq. 1.

$$E = \frac{P}{v_s \times h \times s} \tag{1}$$

Layer thickness is set at s = 20 µm. From a practical point of view, it is extremely challenging to modify layer thickness by only a few micrometers, especially within one build. Hence, laser power, scan velocity, and hatch distance were selected as the input variables to be modified in each treatment. Both sets of coupons, built with SSR = 90° and ≈67° scanning rotation between layers, were measured for size and mass to determine the density of each coupon. The mass of the coupon was calculated using a weighing scale. The volume of the coupon was calculated by measuring the length, width, and height of the coupon using a manual Coordinate Measurement Machine. All test coupons were measured for relative density and found to be between 96 and 99 %.

Fabricated test coupons are 16 mm × 16 mm × 15 mm in dimension. Due to the wire electrical discharge machining (EDM) process used to remove the finished coupons from the base plate, the final height of the coupons are less than 15 mm. Coupons are processed with 4-mm stripes, with a 0.1-mm overlap between each stripes. Process parameters follow the Box-Behnken design with ranges such that the resulting energy density coincides with the acceptable builds shown in [2]. The selected Box-Behnken design requires 15 coupons to be processed with distinct parameters, as well as three additional replications at the default setting (P = 195 W, v_s = 800 mm/s, h = 0.10 mm). The rotation angle scan strategy was not included as a factor in the design; rather, two separate designs were made for SSR = 90° and ≈67° rotation strategies, with otherwise identical parameters. Therefore, 36 coupons were built in total for the experiments. It is important to note that the SSR = 67° scan strategy setting is the recommended setting for the L-PBF machine.

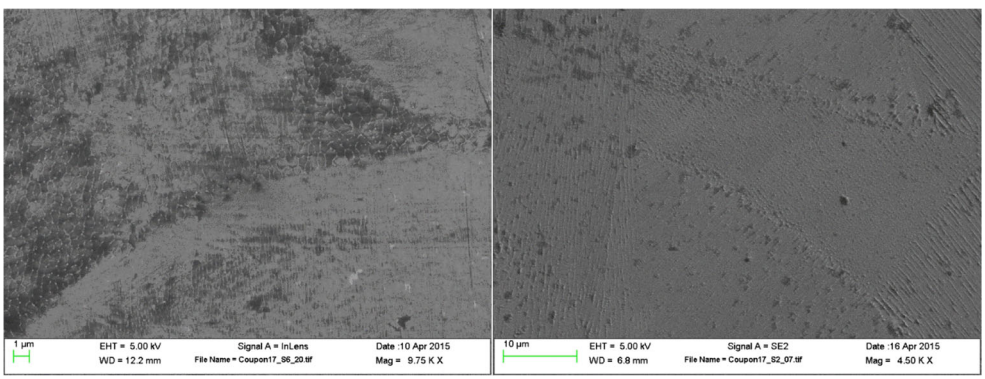

Fig. 8 SEM image of horizontal (XY) section (*left*) and vertical (YZ) section (*right*) of IN625 coupon (P = 182 W, v_s = 800 mm/s, h = 0.10 mm, SSR = 90°) showing cellular growth between meltpool regions and columnar growth within meltpool regions

2.1 Microstructure analysis

In order to analyze the microstructure of L-PBF processed IN625, specimens have been prepared as explained in the next sections. Due to the nature of the L-PBF process, processed layers are reheated many times during the processing of new layers, and the effect of reheating on the microstructure can only be observed from the interior layers. Moreover, because of relatively lower thermal conductivity of the surrounding powder compared to the solid part, the outside contour of the coupons experience a lower cooling rate than the core due to the lower conductivity of the surrounding powder which will also affect the microstructure. Furthermore, the L-PBF machine processes the outer edges of the specimens with different parameters than used in the core of the part. Therefore, coupons obtained via L-PBF were first ground to remove approximately 500 μm from the outside surfaces. After the grinding operation, the L-PBF coupons were electropolished to reveal the microstructure. SEM images were obtained from the prepared test coupons using the InLens and secondary electron (SE2) detectors, from XY, XZ, and YZ surfaces at multiple locations and magnification levels. Figure 6 shows the XZ view of the IN625 coupon processed with P = 195 W, v_s = 800 mm/s, h = 0.10 mm, SSR ≈ 67°. Here, the build direction (Z) is shown with a white arrow. This coupon is of specific importance as it was processed with the default settings. Layers can be seen approximately 20 μm apart, and the layer thickness varies along each layer as the meltpools intrude and join with the previously solidified layers. Figure 7 shows the XZ view of the coupon at larger magnifications. Columnar grains are observed in the build direction, approximately 0.75 μm in width. These grains are aligned towards the build direction, with inclinations ranging approximately +/−10°. Figure 8 shows the XY and YZ views of IN625 coupon processed with P = 182 W, v_s = 800 mm/s, h = 0.10 mm, SSR = 90°. It is observed that the region between two curved meltpool boundaries contains equiaxed grains, whereas columnar grains as well as equiaxed

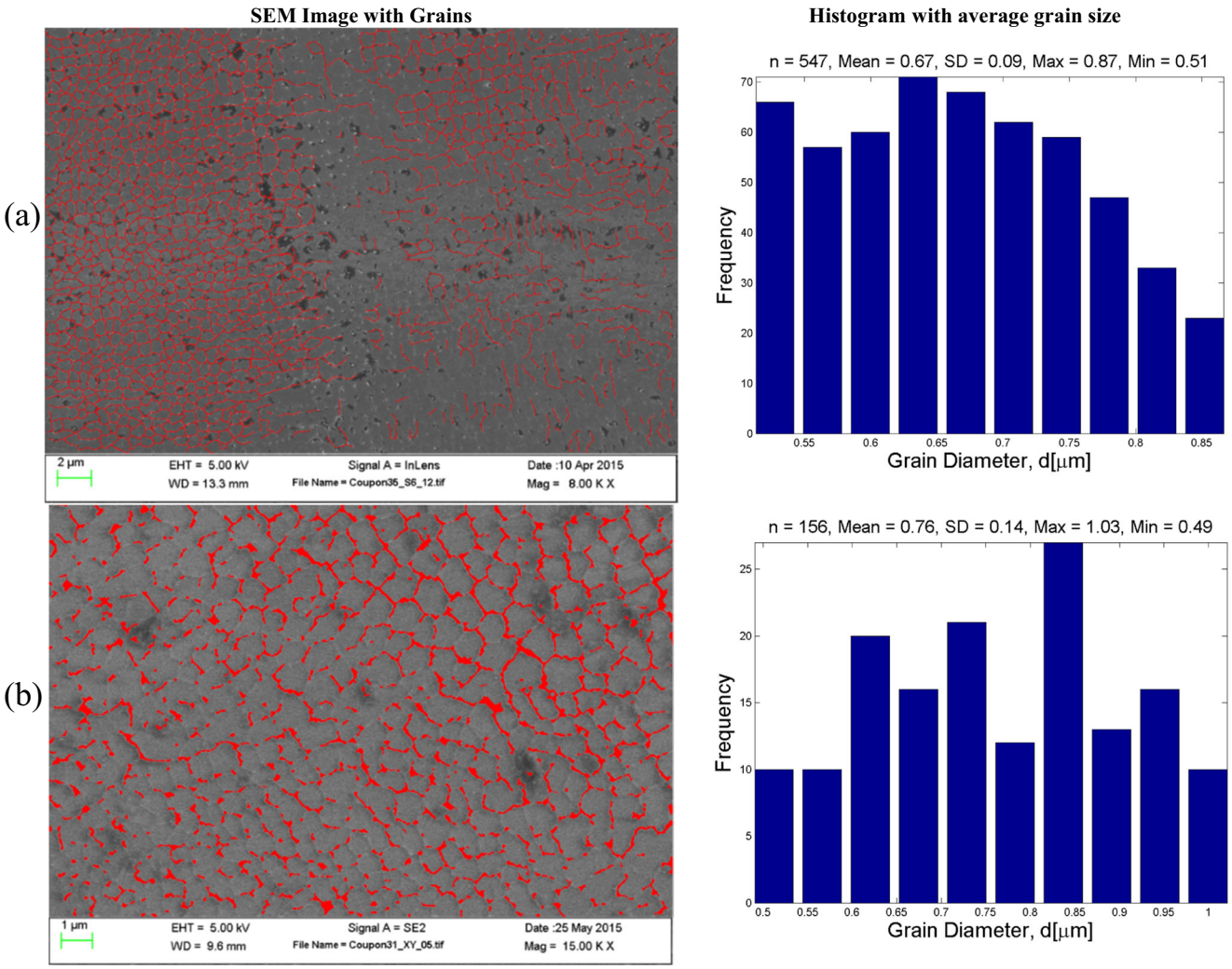

Fig. 9 Grain size analysis of L-PBF processed IN625 coupons, **a** coupon processed with P = 195 W, v_s = 800 mm/s, h = 0.1 mm, SSR = 90° and **b** coupon processed with P = 195 W, v_s = 800 mm/s, h = 0.1 mm, SSR ≈ 67°

Table 1 Processing conditions and grain size analysis results for 90° rotation scan strategy

Coupon #	Rotation strategy SSR (°)	Laser power P (W)	Scan velocity v_s (mm/s)	Hatch distance h (mm)	Energy density E (J/mm^3)	Average grain diameter D_{avg} (μm)	SD of grain diameters SD_{avg} (μm)
1	90	169	875	0.1	96.6	0.68	0.09
4	90	195	875	0.1	111.4	0.56	0.10
6	90	182	875	0.09	115.6	0.49	0.08
8	90	182	725	0.11	114.1	0.47	0.09
9	90	195	800	0.11	110.8	0.52	0.10
12	90	182	725	0.09	139.5	0.75	0.11
14	90	182	800	0.1	113.8	0.66	0.14
15	90	182	800	0.1	113.8	0.49	0.10
16	90	195	725	0.1	134.5	0.71	0.11
17	90	182	800	0.1	113.8	0.66	0.10
18	90	182	875	0.11	94.6	0.51	0.09
20	90	169	725	0.1	116.6	0.62	0.12
21	90	169	800	0.09	117.4	0.55	0.10
23	90	169	800	0.11	96.0	0.56	0.08
29	90	195	800	0.09	135.4	0.65	0.11
35	90	195	800	0.1	121.9	0.67	0.09

grains are observed within the meltpool boundaries. This is a similar result to Fig. 4b, which belongs to the YZ view.

2.2 Measurement of grain size

Grain sizes are indicative of cooling rates and can affect the mechanical properties of the material significantly. An image processing procedure is applied on SEM images in order to calculate the average diameters of the cellular grains commonly seen in the XY plane. High magnifications using 8K to 15K times on the SEM images have been used where needed to reveal the grain shapes and sizes. Marking the grains on each SEM image is a challenging task given the sheer number of grains and images involved. The task is accomplished by utilizing various image analysis methods and machine learning using MATLAB. This process is repeated for 32 coupons on

Table 2 Processing conditions and grain size analysis results for 67° rotation scan strategy

Coupon #	Rotation strategy SSR (°)	Laser power P (W)	Scan velocity v_s (mm/s)	Hatch distance h (mm)	Energy density E (J/mm^3)	Average grain diameter D_{avg} (μm)	SD of grain diameters SD_{avg} (μm)
2	67	169	725	0.1	116.6	0.52	0.12
3	67	195	725	0.1	134.5	0.52	0.11
5	67	169	800	0.09	117.4	0.57	0.09
7	67	182	800	0.1	113.8	0.60	0.08
10	67	182	725	0.11	114.1	0.73	0.13
11	67	169	875	0.1	96.6	0.50	0.09
13	67	195	800	0.09	135.4	0.62	0.09
19	67	195	875	0.1	111.4	0.48	0.21
22	67	182	800	0.1	113.8	0.39	0.15
24	67	182	800	0.1	113.8	0.55	0.15
25	67	195	800	0.11	110.8	0.50	0.09
26	67	182	875	0.09	115.6	0.51	0.07
27	67	182	725	0.09	139.5	0.44	0.15
28	67	182	875	0.11	94.6	0.39	0.06
30	67	169	800	0.11	96.0	0.61	0.14
31	67	195	800	0.1	121.9	0.76	0.14

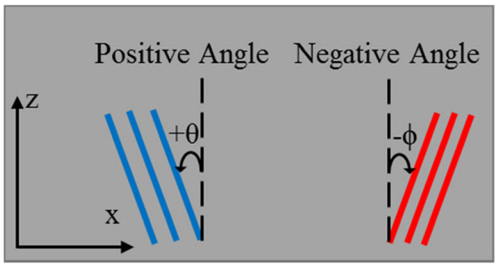

Fig. 10 Positive and negative angles and line coloring

XY surfaces. Note that a standard SEM image consists of 1024 pixels by 768 pixels, and the grayscale color information of each pixel is coded as an integer between 0 and 255. Note that the cellular grains appear to be more elongated on XZ and YZ images, which could be a result of temperature gradients. The number of grains identified in each image varies between 126 and 547, which is sufficient for statistical analysis. Only one image per condition is chosen to be processed and further analysis can yield more general results. Figure 9 shows the grain size measurements from two of the IN625 coupons: (a) coupon processed with P = 195 W, v_s = 800 mm/s, h = 0.1 mm, SSR ≈ 67° rotation and (b) coupon processed with P = 195 W, v_s = 800 mm/s, h = 0.1 mm, SSR = 90° rotation scan strategy. Measurements for all coupons are summarized in Tables 1 and 2, showing average grain diameters

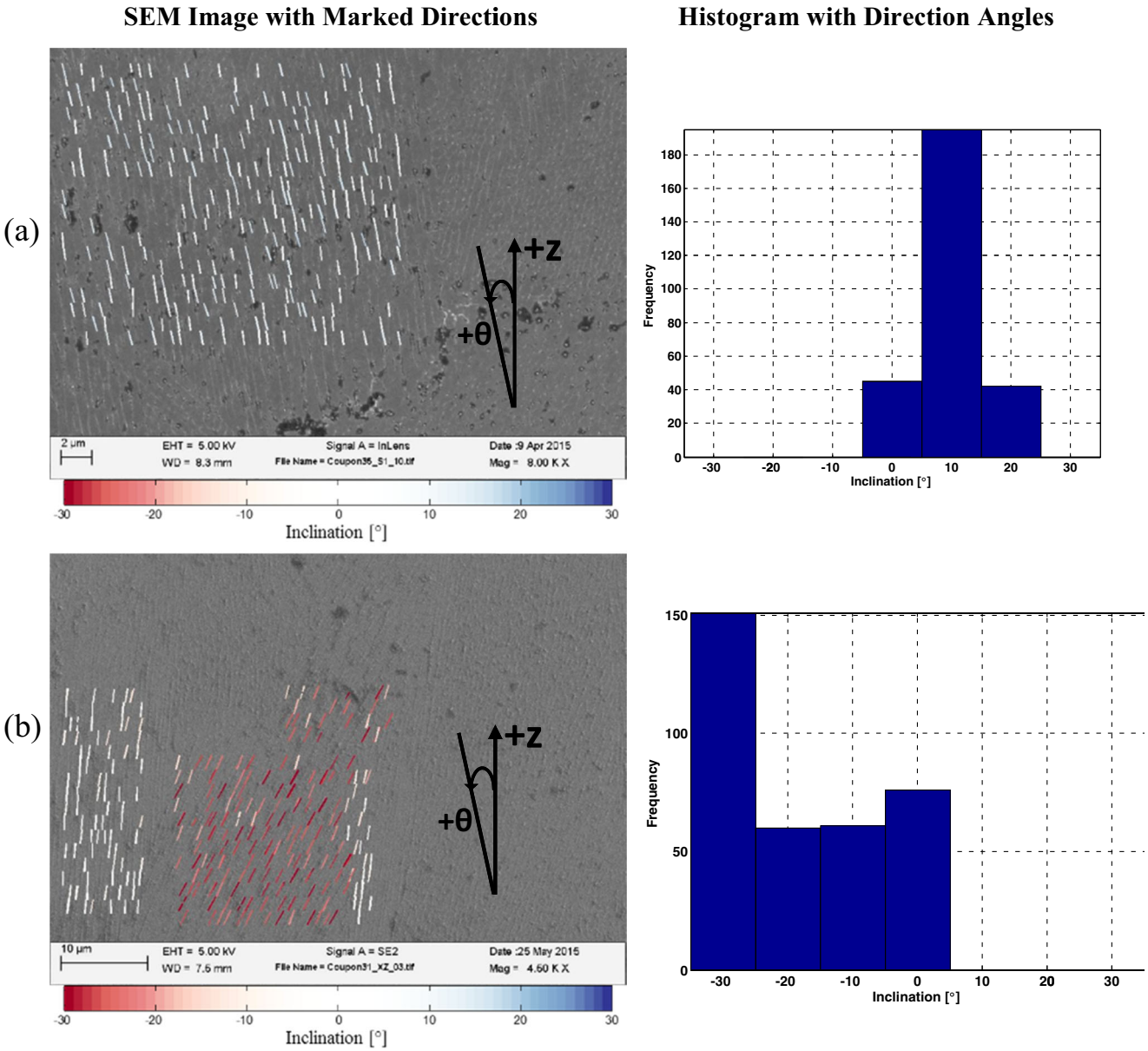

Fig. 11 Growth directions and histograms of inclination angles from the build direction (+Z) for IN 625 test coupons observed from XZ faces, **a** coupon #35 (P = 195 W, v_s = 800 mm/s, h = 0.1 mm, SSR = 90°) and **b** coupon #31 (P = 195 W, v_s = 800 mm/s, h = 0.1 mm, SSR ≈ 67°)

Table 3 Processing conditions and grain growth direction analysis results for 90° rotation

Coupon #	Laser power P (W)	Scan velocity v_s (mm/s)	Hatch distance h (mm)	Energy density E (J/mm^3)	θ+ (°)	Mean of θ+ (°)	SD of θ+ (°)	θ− (°)	Mean of θ− (°)	SD of θ− (°)
1	169	875	0.1	96.6	20	19.3	2.7	−10	−9.5	2.5
4	195	875	0.1	111.4	30	27.8	1.9	−10	−11.5	2.5
6	182	875	0.09	115.6	10	11.7	2.5	0	3.7	1.2
8	182	725	0.11	114.1	20	19.9	2.5	−10	−11.0	2.8
9	195	800	0.11	110.8	30	27.8	1.6	−10	−11.2	2.9
12	182	725	0.09	139.5	0	−1.8	2.3	−10	−10.0	2.6
14	182	800	0.1	113.8	30	27.7	1.7	−10	−9.9	2.6
15	182	800	0.1	113.8	10	10.6	2.7	0	1.4	2.3
16	195	725	0.1	134.5	30	27.6	0.7	−10	−13.2	1.2
17	182	800	0.1	113.8	10	9.8	2.9	−20	−22.2	2.1
18	182	875	0.11	94.6	20	20.0	2.2	−20	−19.8	2.4
20	169	725	0.1	116.6	20	21.1	2.9	0	2.0	2.5
21	169	800	0.09	117.4	0	−0.9	2.8	−10	−9.2	2.4
23	169	800	0.11	96.0	20	18.2	2.5	0	1.2	2.1
29	195	800	0.09	135.4	30	28.0	1.8	−10	−12.1	2.1
35	195	800	0.1	121.9	10	10.6	2.5	0	3.5	1.1

for each coupon, along with the processing conditions. The grain diameter measurement uncertainty from the SEM images is about $u_D = 0.1$ μm, and the average values incorporated >100 resulting $u_{D\text{avg}} = u_{D/\sqrt{100}} = 0.01\mu m$ It is estimated that the measurement uncertainty for the average grain diameters is about $u_{D\text{avg}} = 0.01\mu m$.

2.3 Measurement of growth directions

Growth directions provide valuable information about how the processing parameters affect the microstructure as they are indicative of cooling rates and dominant directions of heat conduction. The images reveal a dendritic microstructure with

Table 4 Processing conditions and grain growth direction analysis results for 67 ° rotation

Coupon #	Laser power P (W)	Scan velocity v_s (mm/s)	Hatch distance h (mm)	Energy density E (J/mm^3)	θ+ (°)	Mean of θ+ (°)	SD of θ+ (°)	θ− (°)	Mean of θ− (°)	SD of θ− (°)
2	169	725	0.1	116.6	10	9.6	2.9	0	−0.6	2.7
3	195	725	0.1	134.5	10	10.2	2.6	0	2.6	2.0
5	169	800	0.09	117.4	10	11.7	2.3	−10	−9.2	2.9
7	182	800	0.1	113.8	20	19.0	2.8	−10	−9.9	2.7
10	182	725	0.11	114.1	20	19.6	3.0	−20	−20.1	2.8
11	169	875	0.1	96.6	20	19.9	2.3	−20	−19.5	2.4
13	195	800	0.09	135.4	10	10.1	2.7	−10	−10.4	2.4
19	195	875	0.1	111.4	0	−3.6	1.4	−10	−12.1	2.2
22	182	800	0.1	113.8	10	12.3	2.0	0	4.4	0.5
24	182	800	0.1	113.8	20	19.3	3.0	10	12.1	2.0
25	195	800	0.11	110.8	30	28.5	1.7	−10	−11.5	2.4
26	182	875	0.09	115.6	30	27.9	1.7	−10	−11.4	2.7
27	182	725	0.09	139.5	30	28.0	1.8	−20	−20.7	2.9
28	182	875	0.11	94.6	10	10.5	2.8	−20	−19.5	2.7
30	169	800	0.11	96.0	30	28.2	1.6	−20	−19.9	3.5
31	195	800	0.1	121.9	0	−2.7	2.0	−30	−27.8	1.5

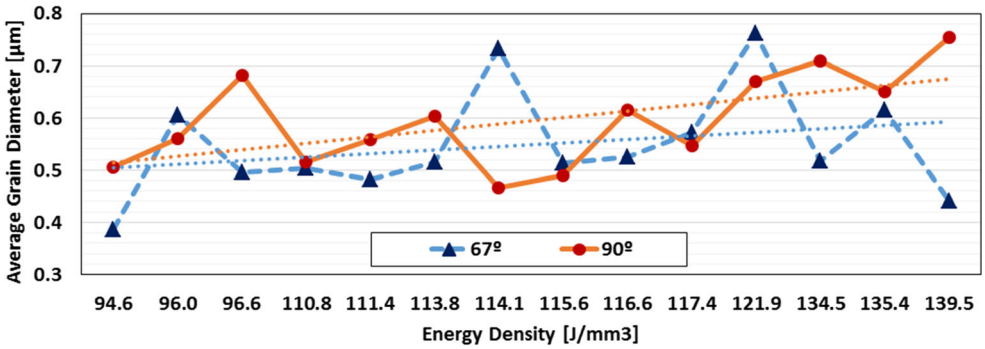

Fig. 12 Effect of energy density (standard deviations for average grain diameter are given in Tables 1 and 2)

cross sections of dendrites appearing as equiaxed grains in different cross sections of the coupons. The dendrites appear to be growing towards cooler areas in two main directions, in the build (Z) direction and also in a direction perpendicular to the laser's scan path. During the processing, the scan path changes many times, thus creating dendrites in different directions. The growth of dendrites in these two directions can be explained by temperature gradients as dendritic growth is observed when the growth is diffusion driven, due to large gradients of temperature or concentration being present. In the case of L-PBF, the temperature gradient is largest in the build direction as the cooling occurs towards the base plate via conduction and towards the environment at the top layer. Analyzing the orientation of the dendrites may reveal the effect of different heating/cooling cycles resulting from process parameters on the microstructure of the IN625.

The growth directions in the different microstructures resulting from different process conditions are identified with image analysis using MATLAB. By looking at the XZ cross section of the test coupons, boundaries of columnar grains are identified and their directions with respect to the Z axis are obtained (Fig.10). Looking at YZ cross sections would also yield similar results due to the rotational scan strategies. After the image processing algorithm detects growth directions in the SEM images, growth angles are calculated. These angles are positive in the counterclockwise direction from the Z axis, as shown in Fig. 9. Lines with positive inclination are shown in blue whereas lines with positive inclination are shown in red. Lines with angles close to 0° appear white and coloring gets stronger with increasing angle magnitude. Coupons were aligned with the SEM detector using coupon edges at the time of recording in order to minimize the error coming from tilting in the images. It is estimated that the alignment error is <1°.

Figure 11 shows the measurements from coupons 35 (P = 195 W, v_s = 800 mm/s, h = 0.1 mm, SSR = 90°) and 31 (P = 195 W, v_s = 800 mm/s, h = 0.1 mm, SSR ≈ 67°). Figure shows histograms, with bin sizes of 10°, of calculated dendrite inclination angles, which are skewed in opposite directions for the two scan rotation strategies. For further analysis, dominant (peak frequency bin) positive and negative directions (where available) are chosen from each image. Measurements for all coupons are summarized in Tables 3 and 4, showing dominant angles as centers of the peak frequency bins as well as averages and standard deviations of angles within those bins for both positive and negative directions, along with the processing conditions.

2.4 Effect of process parameters on grain size

The effects of process parameters on grain sizes are investigated with effect plots, where 67° and 90° rotation strategies are considered separately. Figures 12, 13, 14, and 15 show the main effects of energy density, laser power, scan velocity, and hatch distance on the measured average grain sizes, respectively. In general, increasing the energy density causes an increase in the average grain sizes. Laser power does not seem

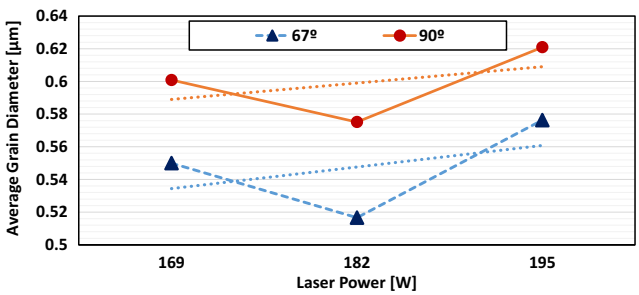

Fig. 13 Effect of laser power (standard deviations for average grain diameter are given in Tables 1 and 2)

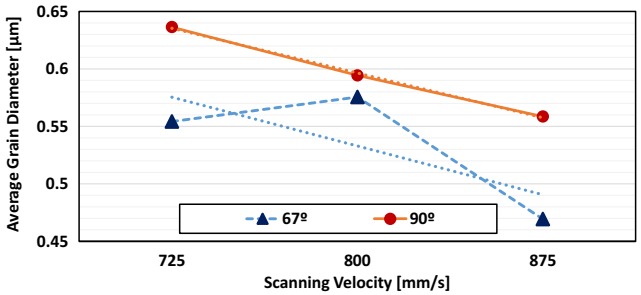

Fig. 14 Effect of scan velocity (standard deviations for average grain diameter are given in Tables 1 and 2)

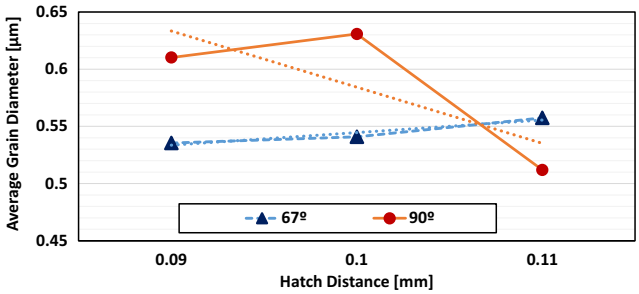

Fig. 15 Effect of hatch distance (standard deviations for average grain diameter are given in Tables 1 and 2)

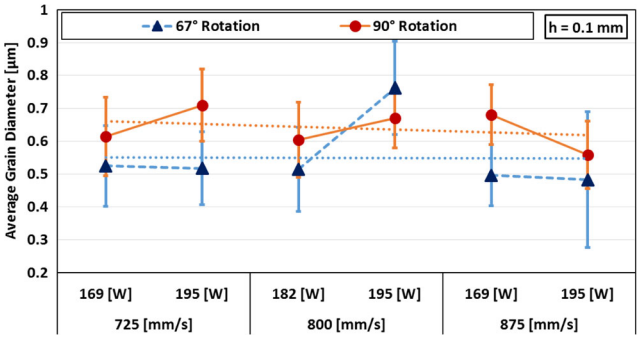

Fig. 17 Effect of scan velocity and laser power

to affect the grain sizes significantly in both 67° and 90° rotation strategies. Increasing scan velocities tends to decrease the grain sizes in both 67° and 90° rotation strategies. Increasing hatch distance tends to reduce the grain average grain diameters in the case of 90° rotation, whereas in the 67° rotation, the change is not as significant.

In order to better understand the effect of each process parameter, a detailed analysis is carried out by looking at effects of two process parameters at different levels while keeping the third process parameter constant at the medium level, as shown in Figs. 16, 17, 18, and 19. In these figures, the error bars represent standard deviations. It is clear that there are many factors affecting the microstructural evolution. Figure 16 shows that at a low laser power, increasing the scan velocity causes an increase in the average grain sizes for 90° rotation strategy and a decrease in the average grain sizes for the 67° rotation strategy. At the high power level (195 W), increasing scan velocity decreases the average grain size for 90° rotation, and a nonlinear effect is observed for the 67° rotation. Figure 17 shows that at low and medium scan velocities, increasing the laser power tends to increase the average grain size for 90° rotation, while at the high scan velocity level, the effect is reversed. For 67° rotation, a clear trend is not observed for low and high velocities, but at the medium velocity, average grain sizes are increased with increasing power. Figure 18 shows that at low and medium hatch distance settings, increasing laser power tends to increase the average grain size for both 67° and 90° rotation strategies while at the high-level hatch distance setting (h = 0.11 mm), increasing power decreases the average grain size for both strategies. Finally, Fig. 19 shows that at the low-level hatch distance setting (h = 0.09 mm), increasing the scan velocity decreases the average grain size for 90° rotation whereas at the high-level hatch distance setting, the effect is reversed. For the 67° rotation strategy, increasing the scan velocity increases the average grain size at the low hatch distance setting but decreases it at the high hatch distance setting. It is important to note the sharp changes in the average grain size (diameter) in Fig. 19 that are caused by large changes in the scan velocity.

2.5 Effect of process parameters on growth directions

Figures 20, 21, and 22 show the main effects of laser power, scan velocity, and hatch distance on positive and negative growth directions. The values are obtained from the histogram bin centers. Note that missing values in these figures means that no dominant direction (positive or negative) was identified for that case. Overall, it is seen that increasing laser power increases the magnitude of both positive and negative dominant angles for the 90° rotation strategy whereas it tends to decrease the positive dominant angle and not affect the negative dominant angle for the 67° rotation strategy. Increasing the scan velocity also causes an increase in both positive and negative dominant angles in the 90° rotation strategy setting, whereas a decrease in the positive angle and an increase in the negative angle are observed for the 67° rotation strategy. Finally, increasing the hatch distance tends to increase both negative and positive dominant angles in both 90° and 67°

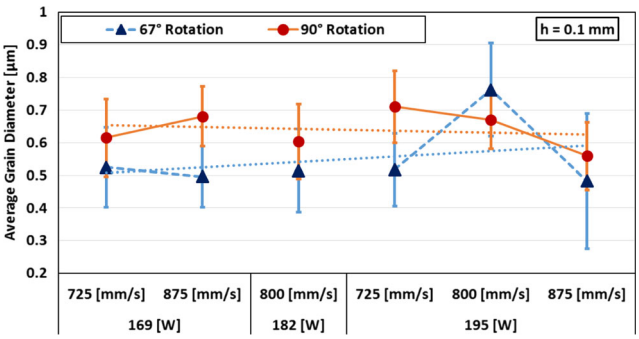

Fig. 16 Effect of laser power and scan velocity

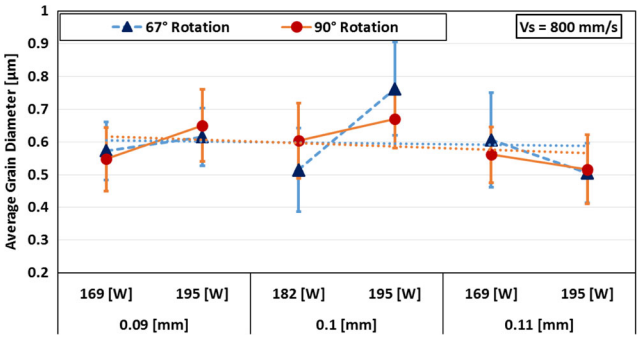

Fig. 18 Effect of hatch distance and laser power

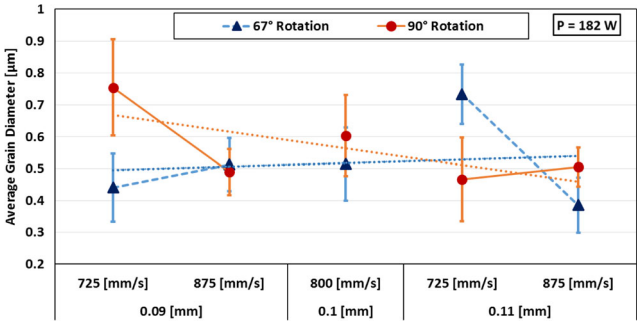

Fig. 19 Effect of hatch distance and scan velocity

rotation strategies. Although the effects are nonlinear in most cases, these plots provide an insight on how the process parameters may alter the microstructure.

Figure 23 shows the effect of energy density on the growth direction angles using the means of the measured angles inside their respective dominant bins. The vertical error bars represent standard deviations of the angles within those bins. An overall decrease in magnitude is observed with increasing energy density in both positive and negative angles, suggesting that as the energy density increases, the grains tend to grow closer to the Z (build) direction. However, the effect is highly nonlinear. Note that the 0° growth direction is considered positive in certain cases and negative in some other cases. Since the bin sizes were 10°, each bin contained samples within the ±5° range of the bin center.

Each process parameter (laser power, scan velocity, and hatch distance) is further investigated in more detail by taking into account the effect of another parameter, while keeping the third one constant as shown in Figs. 24, 25, 26, and 27. Means and standard deviations of the measurements falling into dominant bins in histograms are utilized in these figures. Figure 24 shows that for 90° rotation and at the low power setting, the magnitude of θ− increases with increasing scan velocity while θ+ is not affected significantly. At the high power setting, both θ− and θ+ have nonlinear responses. For 67° rotation, magnitudes of both θ− and θ+ increase with increasing scan velocities at the low power setting. At the high power setting, a decreasing trend is observed for θ+ and a nonlinear trend is observed for θ−.

Figure 25 shows very clear trends at different laser power and scan velocities at 90° rotation. Magnitudes of both θ+ and θ− increase with increasing power at low and high scan velocity conditions. However, both θ+ and θ− magnitudes decrease with increasing power at the medium scan velocity. For 67° rotation, both θ+ and θ− are unaffected by laser power changes at low scan velocity. A decrease in magnitude is observed for θ+ at medium and high velocities with increasing power. The magnitude of θ− increases with increasing power at medium scan velocity and decreases at high scan velocity.

Figure 26 shows that at low hatch distance and with increasing laser power, a significant increase in the dominant positive and negative angles are observed at 90° degree rotation strategy, whereas the 67° degree rotation strategy does not affect the growth directions significantly. A decrease in positive and negative angles is seen in the 90° degree rotation strategy with increasing power. For the 90° degree rotation strategy, an increase in power yields significantly larger negative angles (in magnitude) at the medium hatch distance setting. Finally, at the high hatch distance setting, both positive and negative dominant angles increase in magnitude with increasing power for 90° degree rotation strategy. For the 67° degree rotation strategy, the positive angle is not affected with increasing power while the negative angle gets smaller in magnitude.

Figure 27 shows that at low hatch distance setting, the positive dominant angle increases with increasing velocity for the 90° rotation strategy, while there is no significant change in the 67° rotation strategy. The negative dominant angle decreases in magnitude with increasing velocity at low hatch distance setting for both 90° and 67° rotation strategies. At high hatch distance setting, the positive dominant angles decrease with increasing velocity for the 90° rotation strategy. For the 90° rotation strategy, the negative dominant angle

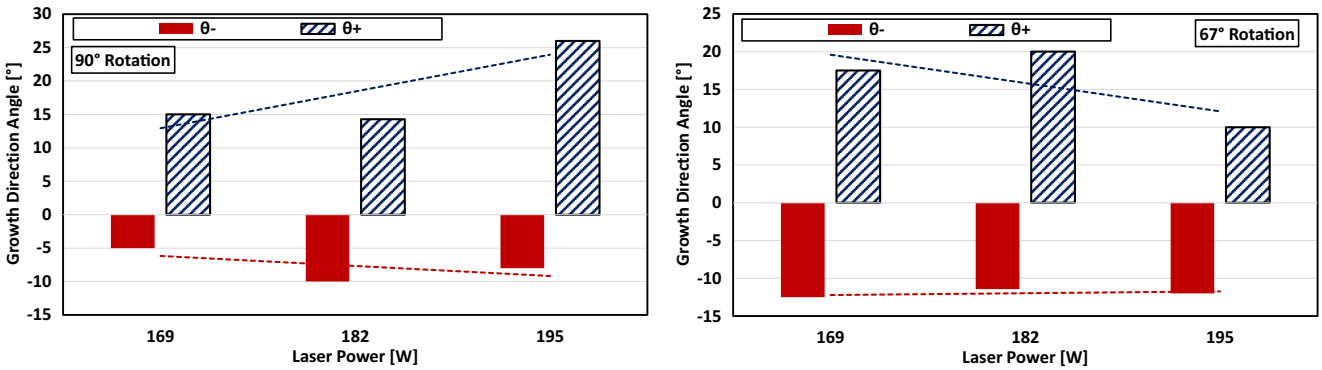

Fig. 20 Effect of laser power on dominant positive and negative growth directions, with 90° (*top*) and 67° (*bottom*) rotation strategies (standard deviations for growth directions are given in Tables 3 and 4)

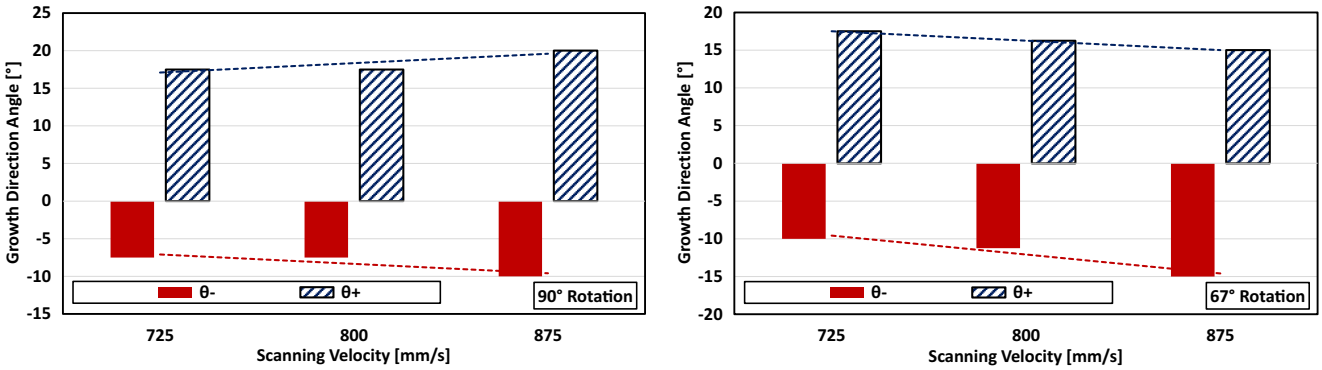

Fig. 21 Effect of scan velocity on dominant positive and negative growth directions, with 90° (*top*) and 67° (*bottom*) rotation strategies

increases in magnitude with increasing velocity but no significant effect was observed at the 67° rotation strategy.

3 Modeling and optimization

3.1 Predictive modeling

A second-order regression model is utilized to establish the input-output relationship between response and controllable process variables efficiently. A quadratic model has the form:

$$y = \beta_0 + \sum_{i=1}^{k} \beta_i x_i + \sum_{i \neq j=1}^{k} \beta_{ij} x_i x_j + \sum_{i=1}^{k} \beta_{ii} x_i^2 + \varepsilon \qquad (2)$$

where y is the response (average grain size or growth direction in our case), x_i are the input variables (process variables), β is the coefficient, and ε is the error. After substituting the response and input variables, the equation becomes:

$$D_{\text{avg}} \text{ or } \theta = \beta_0 + \beta_1 P + \beta_2 v_s + \beta_3 h + \beta_{11} P + \beta_{22} v_s + \beta_{33} h + \beta_{12} P v_s + \beta_{13} P h + \beta_{23} v_s \text{h} + \varepsilon \qquad (3)$$

where D_{avg} (mm) is the average grain size, θ (°) is the positive or negative grain growth direction angle, P (W) is the laser power, v_s (mm/s) is the laser scan velocity, and h (mm) is the hatch distance. It should be noted that overall regression models without quadratic terms have given higher coefficient of determination, R^2.

The coefficients of the regression models were determined using Minitab software and are listed in Table 5 along with calculated coefficients of determination, R^2. Overall, the model provides an acceptable fit. However, it is important to note that in some cases, the R^2 values are not very high, and these results should be utilized with caution. The regression models for θ+ and θ− are visualized with 3D surface plots, showing the response with two main effects, keeping the third factor constant at the medium value. Figure 28 shows the effect of power P and hatch distance h on D_{avg}, θ+ and θ− with 90° and 67° rotation strategies while the scan velocity v_s is kept constant at 800 mm/s. Note that a comparison can be easily made between the 90° and 67° rotation strategies by comparing the figures on the left to those on the right. Figure 29 shows the effect of scan velocity v_s and hatch distance h on D_{avg}, θ+, and θ− with 90° and 67° rotation strategies while the laser power P is kept constant at 182 W. Figure 30 shows the effect of laser power P and scan v_s on D_{avg}, θ+, and θ− with 90° and 67° rotation strategies while the hatch distance h is kept constant at 0.1 mm.

3.2 Single-objective optimization

The process parameters can be optimized in order to obtain a more desirable microstructure. For instance, minimizing the

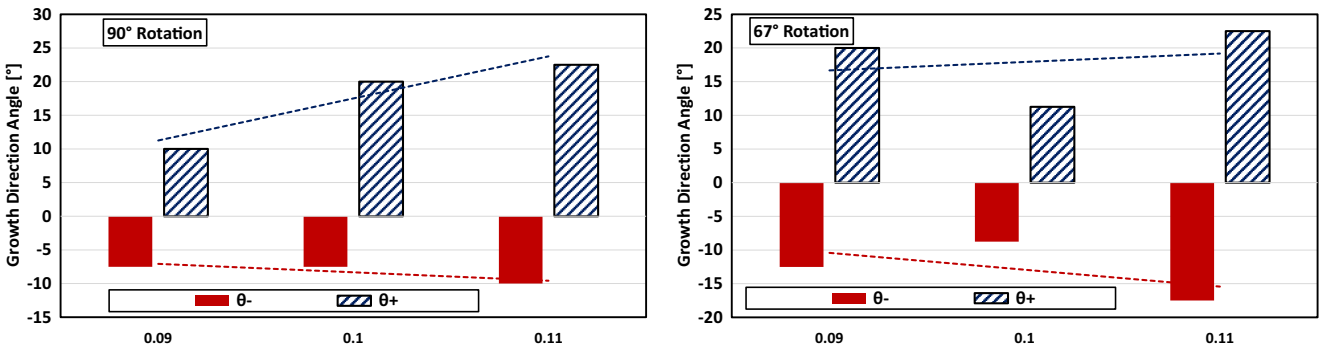

Fig. 22 Effect of hatch distance on dominant positive and negative growth directions, with 90° (*top*) and 67° (*bottom*) rotation strategies

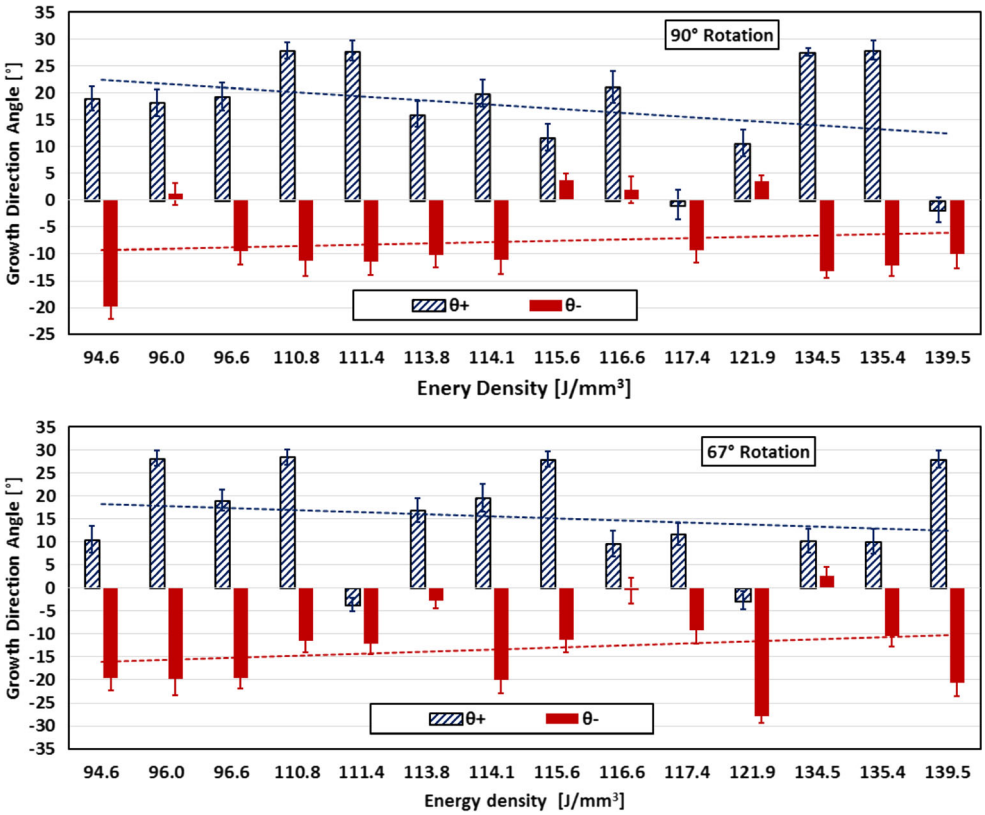

Fig. 23 Effect of energy density on dominant positive and negative growth directions, for 90° (*top*) and 67° (*bottom*) rotation strategies

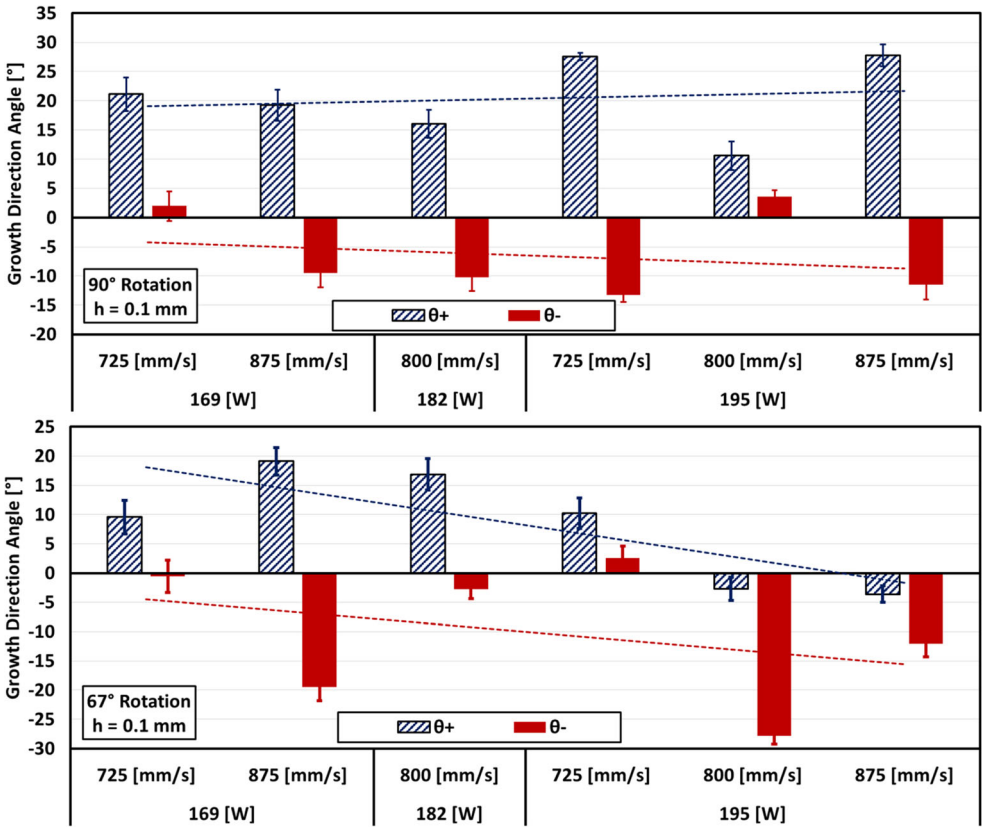

Fig. 24 Effects of laser power and scan velocity on dominant positive and negative growth directions at constant hatch distance (h = 0.1 mm), for 90° (*top*) and 67° (*bottom*) rotation strategies

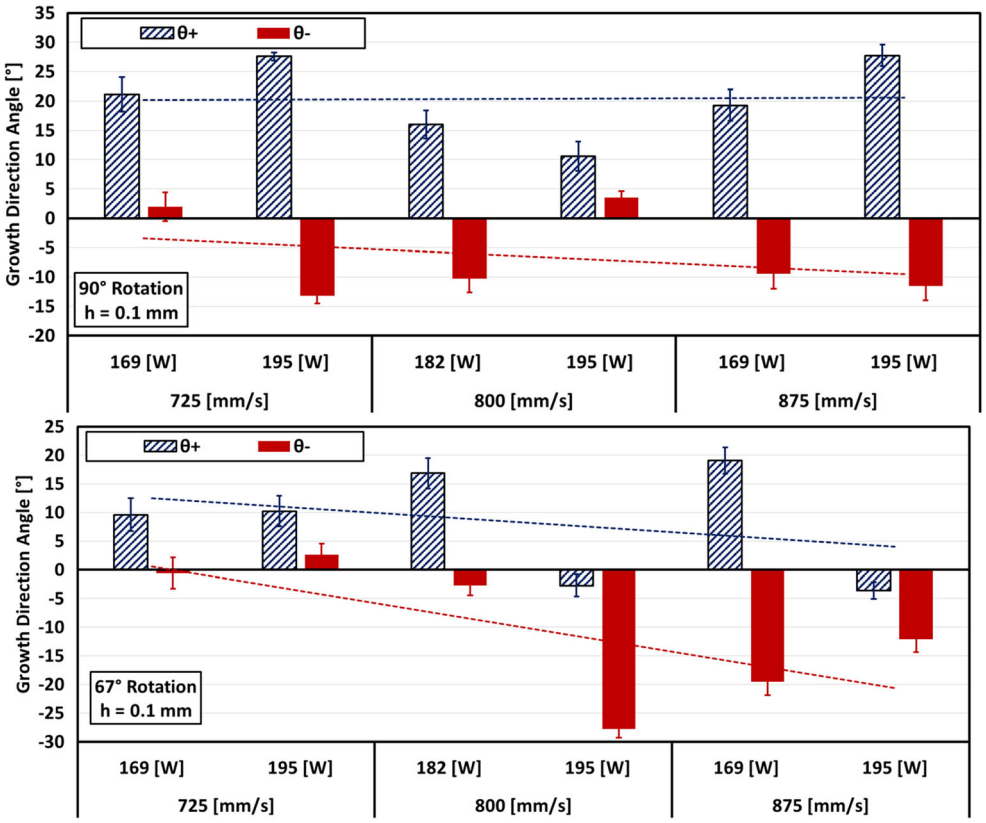

Fig. 25 Effects of scan velocity and laser power on dominant positive and negative growth directions at constant hatch distance (h = 0.1 mm), for 90° (*top*) and 67° (*bottom*) rotation strategies

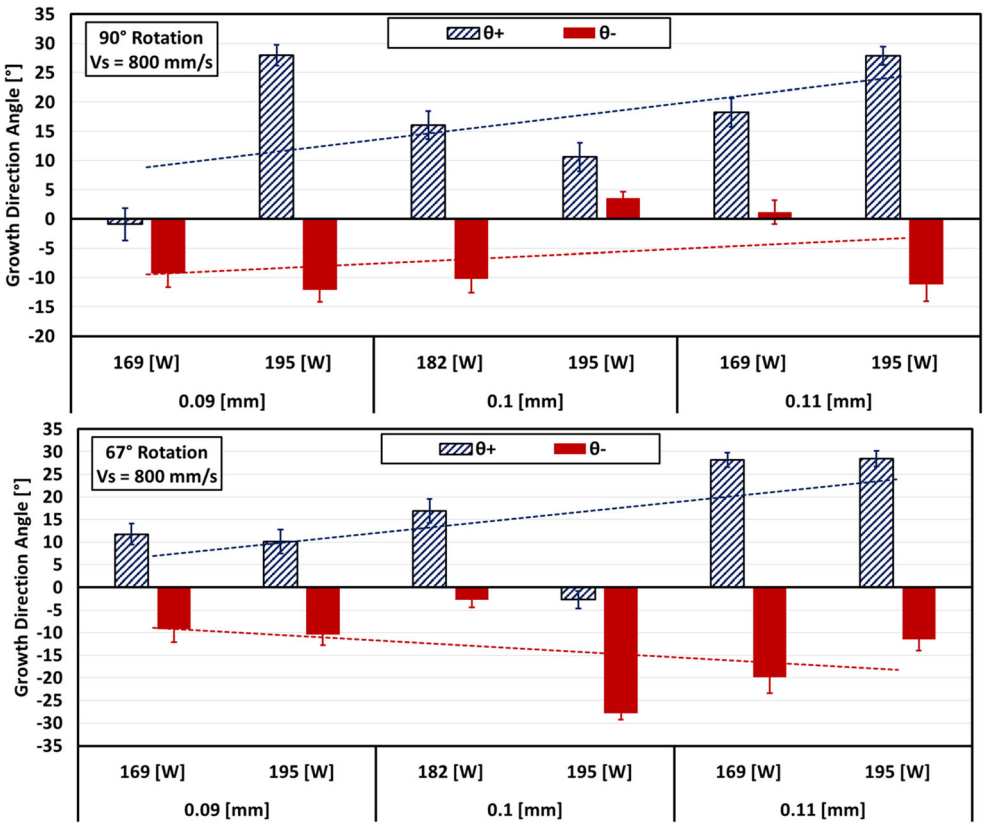

Fig. 26 Effects of hatch distance and laser power on dominant positive and negative growth directions at constant scan velocity (v_s = 800 mm/s), for 90° (*top*) and 67° (*bottom*) rotation strategies

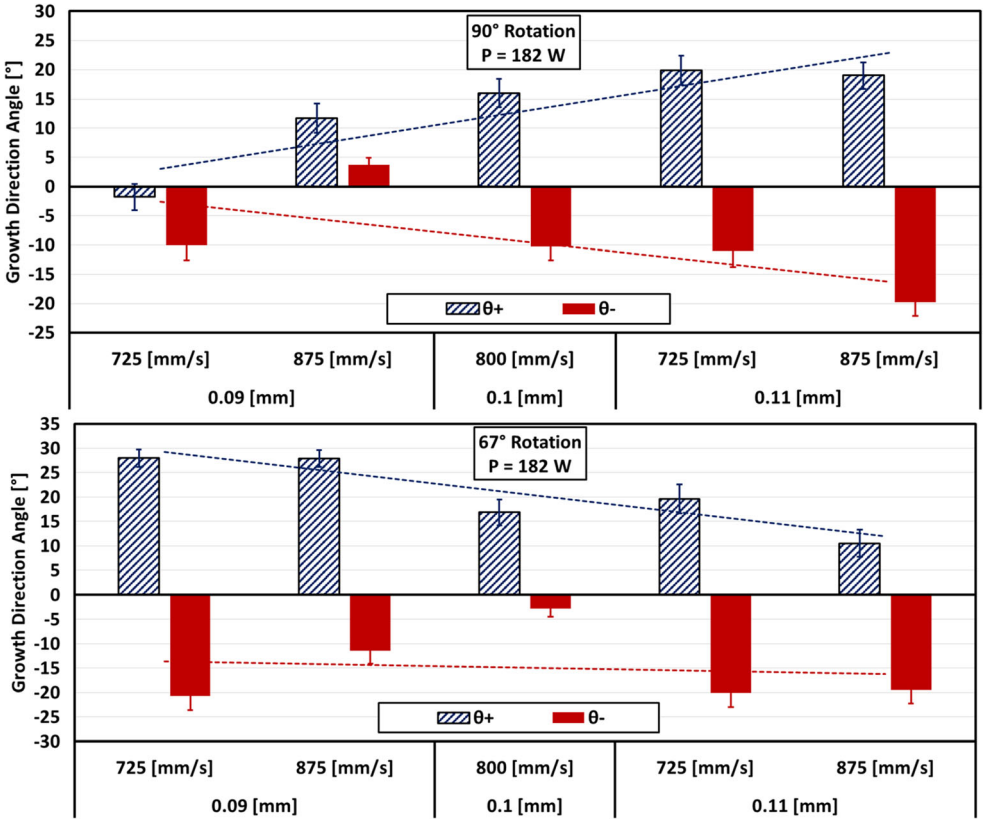

Fig. 27 Effects of hatch distance and scan velocity on dominant positive and negative growth directions at constant laser power ($P = 182$ W), for 90° (*top*) and 67° (*bottom*) rotation strategies

magnitude of growth direction angles and aligning them with the build direction may strengthen the parts in the build direction. A more refined microstructure with smaller grains or larger grain sizes can also be obtained by optimizing the process parameters towards the desired objective. Therefore, we explore the optimum L-PBF process parameters for both refining and coarsening grain sizes by selecting minimization and maximization of average grain diameter as objectives for both scan strategies.

Single-objective optimization is performed on the response surfaces using Minitab, for different objectives such as minimizing or maximizing the average grain size, or grain growth direction angles. Multiple objectives can be combined together in a weighted sum approach to allow simultaneous optimization. In this case, the optimum solutions for each variable may not be as good as the optimum solutions obtained for these variables individually, since an overall solution is

Table 5 Summary of model parameters for the response

	90° rotation scan strategy			67° rotation scan strategy		
Parameter	D_{avg} (mm)	θ+ (°)	θ− (°)	D_{avg} (mm)	θ+ (°)	θ− (°)
β_0	−3.4	−134	82	−10.9	−1531	−2263
β_1	0.0172	−11.26	−5.1	−0.022	14.9	2.3
β_2	−0.0038	0.14	0.02	0.023	2.24	2.15
β_3	88.5	20,664	8004	90	−13,611	24,229
β_{11}	0.000154	0.0414	0.0107	0.000139	−0.0294	−0.0132
β_{22}	0.000002	0.000163	0.000065	−0.000006	−0.00055	−0.00131
β_{33}	−614	−47,432	5879	366	77,397	−127,495
β_{12}	−0.000056	0.00052	0.00338	−0.000002	−0.00599	0.00109
β_{13}	−0.285	−37	−18.3	−0.277	3.6	18.4
β_{23}	0.1015	−4.8	−7.51	−0.1399	−3.02	−2.9
R^2	0.79	0.78	0.44	0.68	0.54	0.66

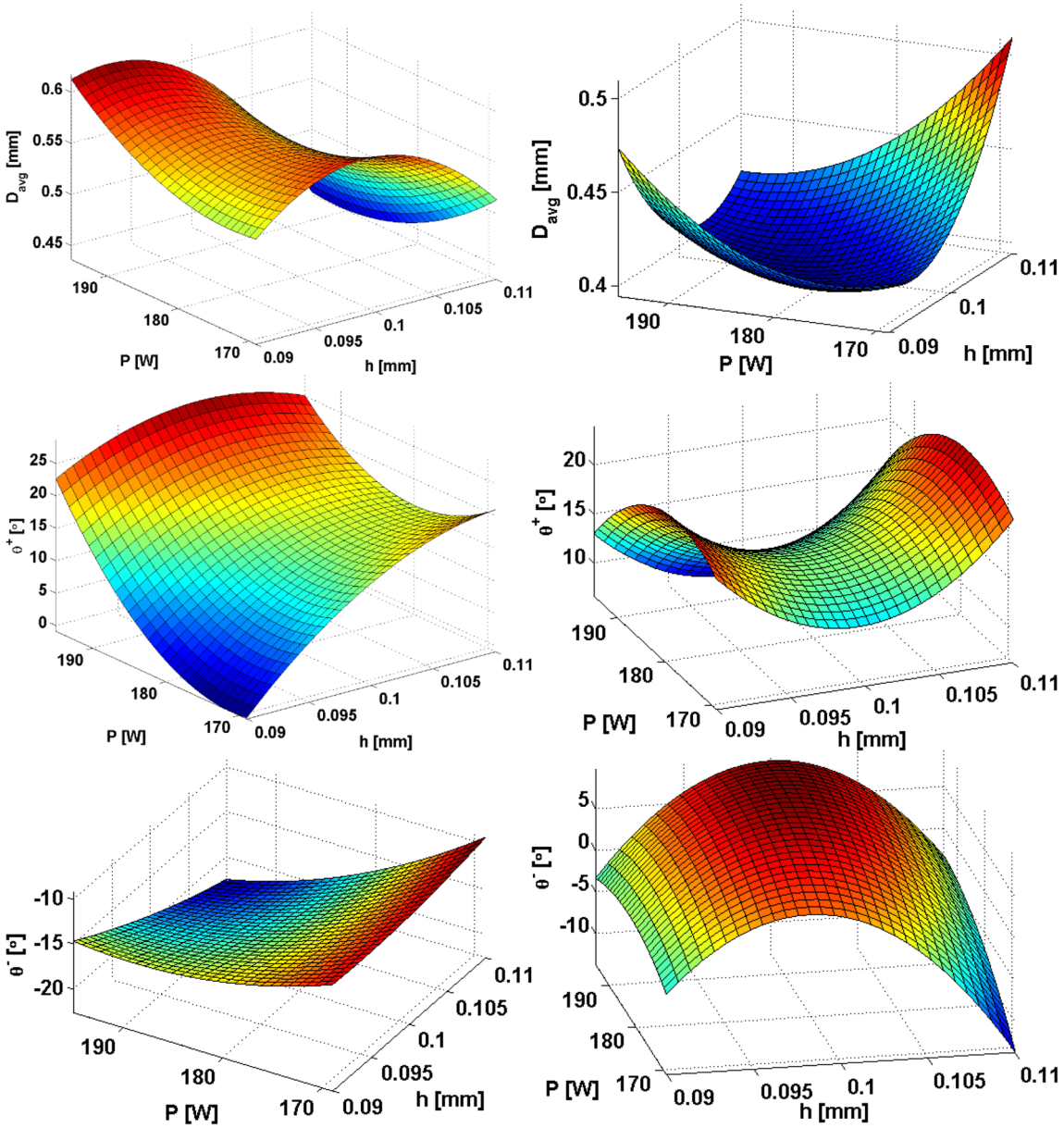

Fig. 28 Surface plots showing the effect of power (P) and hatch distance (h) on grain size (D_{avg}) (*top*), growth directions of θ+ (*middle*) and θ− (*bottom*) with 90° (*left*) and 67° (*right*) rotation strategies. Here, scan velocity (v_s) is kept constant at 800 mm/s

obtained. The decision variables are the process parameters P, v_s, and h.

Various different optimization problems are considered in Minitab, in three different sets. The first set consists of six problems and focuses on the optimization of average grain sizes obtained by 90° and 67° rotation strategies, denoted $D_{avg,90}$ and $D_{avg,67}$, respectively. First, $D_{avg,90}$ and $D_{avg,67}$ are simultaneously minimized with equal importance. Next, the same objective is used for maximization. Additionally, the $D_{avg,90}$ and $D_{avg,67}$ are minimized and maximized individually. The second and third sets consider two problems each, aimed towards optimizing the grain growth direction angles on samples processed with 90° and 67° rotation strategies, respectively. In the second set, target values of 0° are used in optimizing the θ_{90}^{+} and θ_{90}^{-} angles, in order to align the grain growth directions with the build direction thus promoting an anisotropic structure. Furthermore, the magnitudes of θ_{90}^{+} and θ_{90}^{-} are maximized simultaneously so that the growth angles are directed away from the build direction. The third set is identical to the second set, except it utilizes the 67° rotation strategy rather than 90°. The decision variables are constrained to their respective maximum and minimum values used in the process.

When there are multiple response variables (such as grain size and grain orientation), the optimization can be performed by defining the objective function in terms of

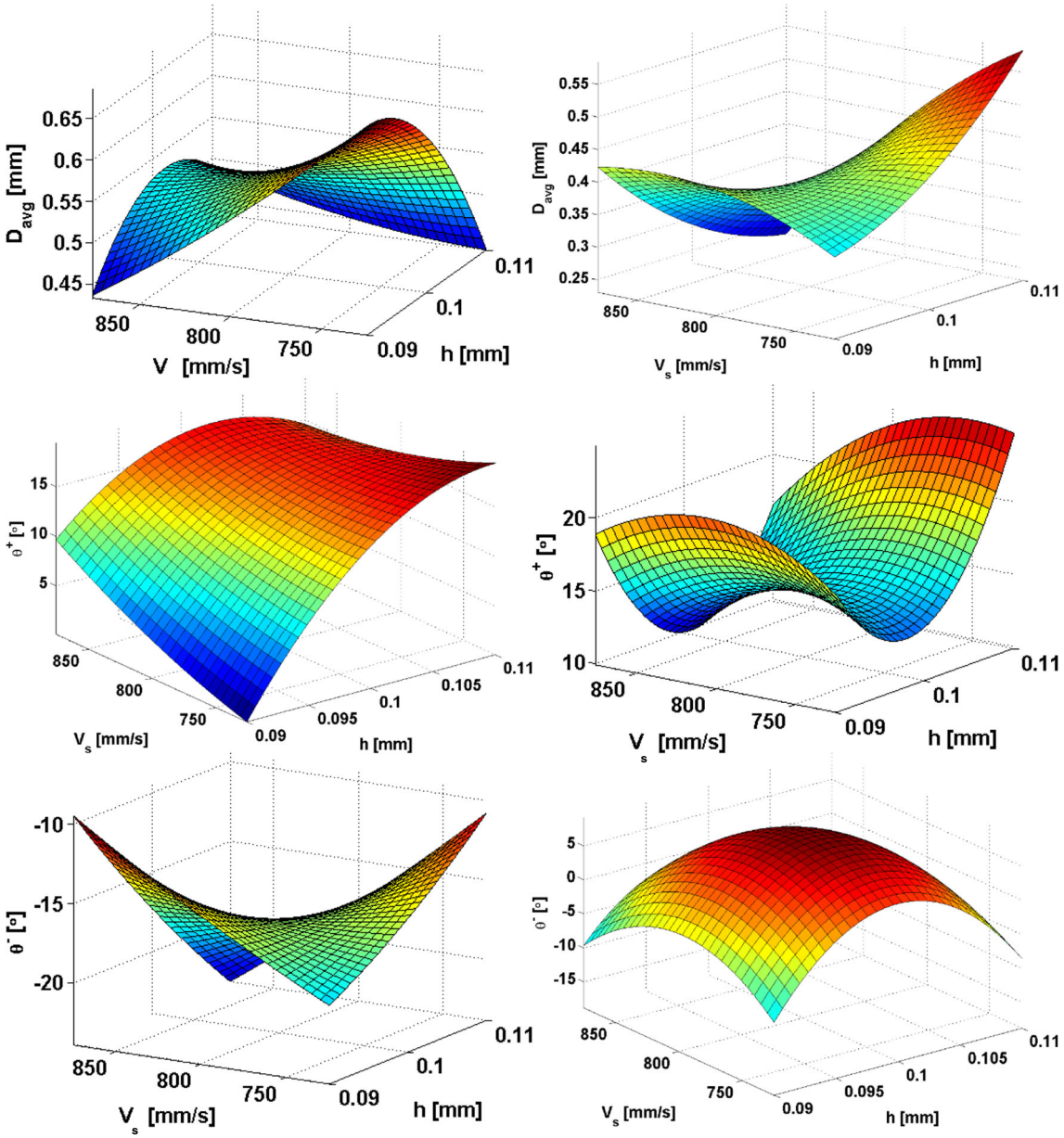

Fig. 29 Surface plots showing the effect of scan velocity (v_s) and hatch distance (h) on grain size (D_{avg}) (*top*) and growth directions of θ+ (*middle*) and θ− (*bottom*) with 90° (*left*) and 67° (*right*) rotation strategies. Here, laser power (P) is kept constant at 182 W

desirability associated with these response variables. The desirability d_i of response variable i with response $Y_i(\boldsymbol{x})$, lower bound L_i, upper bound U_i, and target T_i is defined for three cases in Table 6. Measured grain diameter ranges are used as proper lower bound and upper bound values. In the best target case, the target T_i is the value that the optimization problem attempts to make the response achieve. In maximization and minimization cases, the target T_i is set to relatively high and low values, respectively, in terms of response. The desirability parameters used are given in Table 6, and linear objective functions are assumed.

In the case of multiple objectives, a composite desirability function can be used:

$$D = \prod_i \left(d_i^{w_i}\right)^{1/\sum_i w_i} \tag{4}$$

where w_i is the weight or importance of variable i. In this study, $w_i = 1$ is used, giving equal importance to each response variable.

Tables 7, 8, and 9 show the results of the three sets optimizations performed in Minitab using the desirability functions. For each different objective, the optimum values for the

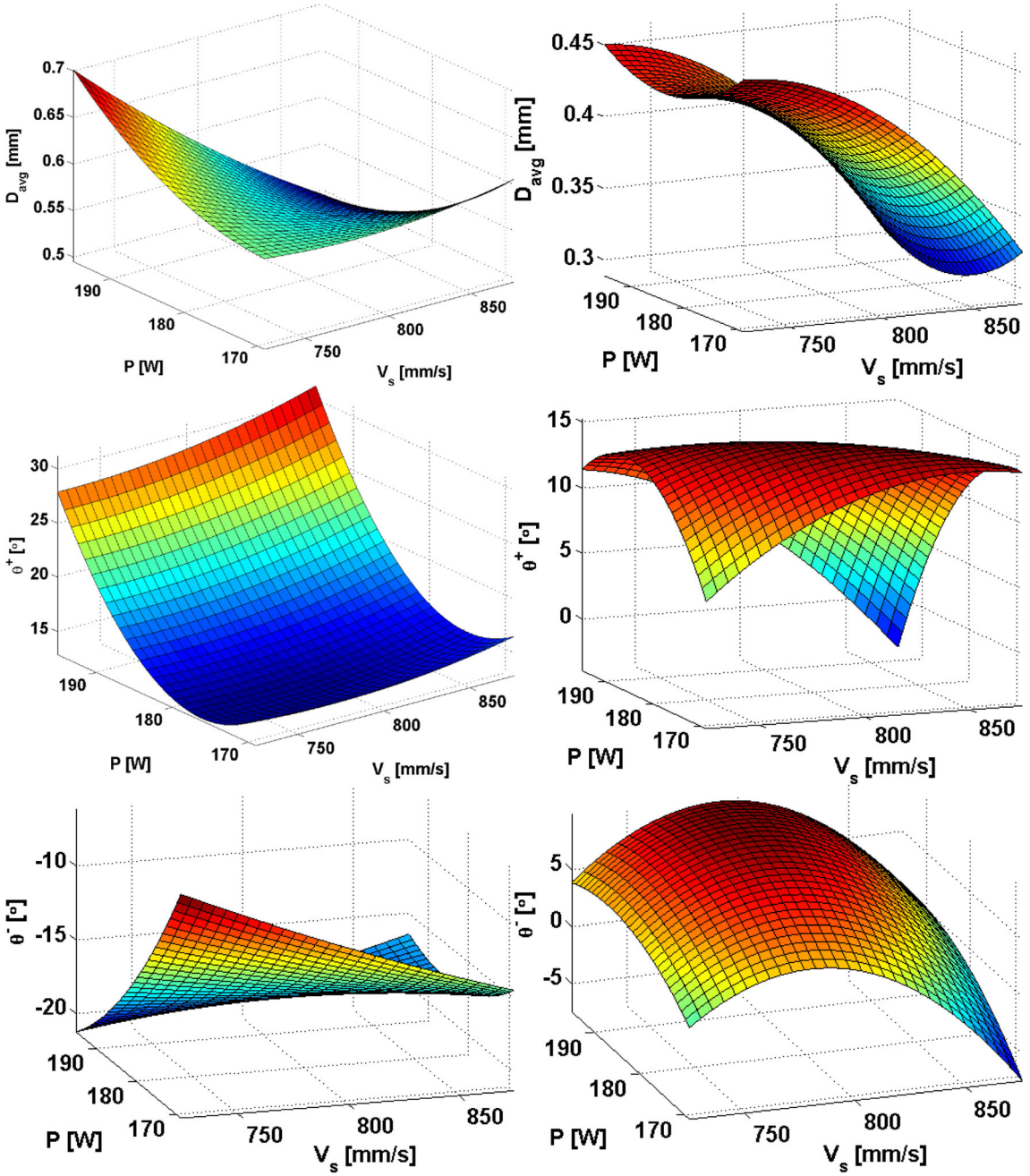

Fig. 30 Surface plots showing the effect of laser power (P) and scan (v_s) on average grain size (D_{avg}) (*top*) and growth directions of θ+ (*middle*) and θ− (*bottom*) with 90° (*left*) and 67° (*right*) rotation strategies. Here, the hatch distance (h) is kept constant at 0.1 mm

responses are reported along with the decision variables. Table 7 shows the first set of optimization results, for average grain sizes $D_{avg,90}$ and $D_{avg,67}$. Individual maximization or minimization of $D_{avg,90}$ and $D_{avg,67}$ require different

Table 6 Desirability function for three different problem types: predefined best target, maximization, and minimization

Predefined best target	$d_i = \{0 \quad , \quad Y_i(x) < L_i \;\; [(Y_i(x)-L_i)/(T_i-L_i)]\,, L_i \le Y_i(x) \le T_i \;\; [(Y_i(x)-U_i)/(T_i-U_i)]\,, T_i \le Y_i(x) \le U_i \;\; 0, \quad Y_i(x) > U_i$
Maximization	$d_i = \{0 \quad , \quad Y_i(x) < L_i \;\; [(Y_i(x)-L_i)/(T_i-L_i)]\,, L_i \le Y_i(x) \le T_i \;\; 1, Y_i(x) > T_i$
Minimization	$d_i = \{1 \quad , \quad Y_i(x) < T_i \;\; [(Y_i(x)-U_i)/(T_i-U_i)]\,, T_i \le Y_i(x) \le U_i \;\; 0, Y_i(x) > U_i$

Table 7 Response surface optimization results

Objective	P (W)	v_s (mm/s)	h (mm)	$D_{avg,90}$ (mm)	$D_{avg,67}$ (mm)
Max. ($D_{avg,90}$, $D_{avg,67}$)	195	758.9	0.09	0.75	0.55
Min. ($D_{avg,90}$, $D_{avg,67}$)	195	865.9	0.11	0.48	0.38
Max. (D_{avg90})	195	725	0.09	0.84	–
Min. ($D_{avg,90}$)	176.6	725	0.11	0.46	–
Max. ($D_{avg,67}$)	169	725	0.11	–	0.75
Min. ($D_{avg,67}$)	195	875	0.11	–	0.36

Table 8 Response surface optimization results for grain growth direction angles θ+ and θ− at 90° rotation strategy

Objective	P (W)	v_s (mm/s)	h (mm)	θ^+_{90} (°)	θ^-_{90} (°)
$T_{\theta^-_{90}} = 0$, $T_{\theta^+_{90}} = 0$	169	786	0.09	0	−4.8
Max. ($-\theta^-_{90}$, θ^+_{90})	195	875	0.109	26.2	−17.8

processing conditions than the combined objective functions, which means that there is no optimum set of process parameters that works with both 90° and 67° rotation strategies. Depending on the objective and the scan strategy, values of P, v_s, and h must be chosen carefully.

Table 8 shows the second set of optimization results, for positive and negative grain growth directions obtained with 90° rotation strategy, θ^+_{90} and θ^-_{90}. There, the different objectives represent two separate quantitative aspects: minimizing the magnitude of positive and negative growth direction angles in order to align them with the z axis to yield an anisotropic structure and maximizing the magnitudes of angles to promote isotropy. Note that the positive angles, θ^+_{90} and θ^+_{67}, have positive values and negative angles, θ^-_{67} and θ^-_{67}, have negative values. By setting a target value of 0 for both positive and negative angles, the angles can be aligned with the build axis as much as possible. This condition is achieved at low power, small hatch distance, and medium-low scan velocity. Conversely, an anisotropic structure is obtained with high power, high velocity, and high hatch distance.

Table 9 shows the third set of optimization results obtained with 67° rotation strategy, for θ^+_{67} and θ^-_{67}. Contrary to the 90° case, high laser power results in an isotropic structure and low power results in an anisotropic structure. A medium-high scan velocity is required for aligning the growth with the build direction, while the high setting is again preferred for the isotropic build. Lastly, a medium hatch distance is required for isotropy while low hatch distance results in the anisotropic structure.

3.3 Multi-objective optimization

In this study, quadratic response functions with interactions as nonlinear models obtained through RSM are used to model the process responses in L-PBF of nickel alloy 625. It is possible to use standard numerical procedures since no local minima or discontinuities of the responses are expected in the presence of quadratic models. However, genetic algorithm (GA) optimization as a popular strategy to optimize nonlinear systems with a large number of variables was used. Especially, moving towards multi-objective optimization, the GA-based solution methods provide distinct advantages for finding a set of feasible solutions to the given problem set where there are conflicting objectives [6].

Multi-objective optimization provides a tool to compare various objectives in complex manufacturing processes as demonstrated by Thepsonthi & Özel [21] and Ulutan & Özel [22]. When more than one objective is considered, especially those that are in conflict with each other, multi-objective optimization can be utilized to reveal the set of best optimal

Table 9 Response surface optimization results for grain growth direction angles θ+ and θ− at 67° rotation strategy

Objective	P (W)	v_s (mm/s)	h (mm)	θ^+_{67} (°)	θ^-_{67} (°)
$T_{\theta^-_{67}} = 0$, $T_{\theta^+_{67}} = 0$	195	835.6	0.0996	4.7	−0.4
Max. ($-\theta^-_{67}$, θ^+_{67})	169	875	0.09	25.2	−19.4

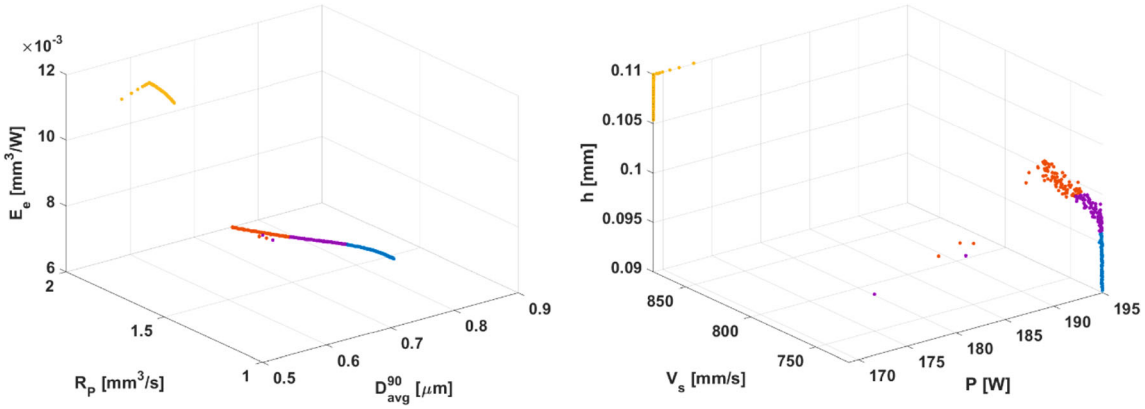

Fig. 31 Multi-objective Genetic Algorithm optimization at the end point for maximization of $D_{avg,90}$, R_p, and E_e with objective values (*left*) and the decision variables (*right*)

solutions, known as the Pareto frontier. Multi-objective Genetic Algorithm optimization (MOGA) [6] is used for multi-objective optimization. Genetic Algorithm (GA) is an evolutionary programming method that mimics the evolution and natural selection process seen in the nature. Starting with an initial population, individuals of the population mate and evolve towards the optimum solution. Each individual in the population has a chromosome that represents the current values of the decision variables for that individual. The next generation of individuals containing the offspring is obtained from the current generation, the parents. The algorithm relies on three main operations: Selection, Crossover, and Mutation. A child (offspring) must be the product of either crossover or mutation. Population-based (multi-parent) algorithms such as Genetic Algorithms [17] are superior to single-solution algorithms such as Tabu Search and Simulated Annealing in terms locating the global optimum, at the cost of convergence speed.

It is known that slow processing rates are a major drawback for the L-PBF process. In order to account for, and improve the processing rates, we define the response, processing rate R_p (mm^3/s) as:

$$R_p = v_s \times h \times s \tag{5}$$

where $s = 0.02$ mm is the layer thickness, which is considered constant for every build. The processing rate increases with scan velocity (v_s) and hatch distance (h). Furthermore, we define an efficiency term, E_e (mm^3/J) to quantify the amount of material processed per energy spent as follows:

$$E_e = R_p \big/ P \tag{6}$$

Consequently, the energy efficiency increases with processing rate and decreases with laser power. Furthermore, we define a new term, $\overline{\theta}_r$ (°) with $r \in \{67, 90\}$ to quantify the magnitude of both positive and negative angles together:

$$\theta_r = \frac{\left|\theta_r^+\right| + \left|\theta_r^-\right|}{2} \tag{7}$$

In an explorative study, desired microstructural properties are sought while maximizing processing rate and energy efficiency. Thus, eight multi-objective optimization problems are constructed as follows:

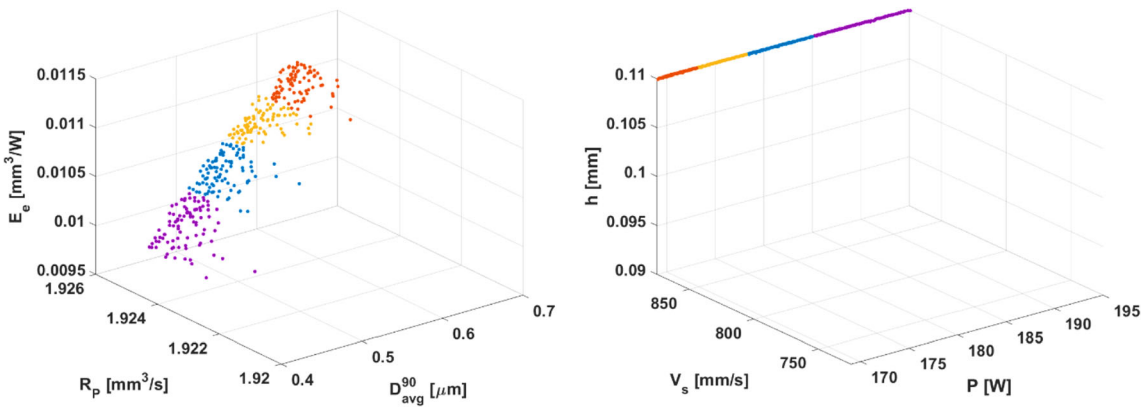

Fig. 32 Multi-objective Genetic Algorithm optimization for minimization of $D_{avg,90}$, and maximization of R_p and E_e with objective values (*left*) and the decision variables (*right*)

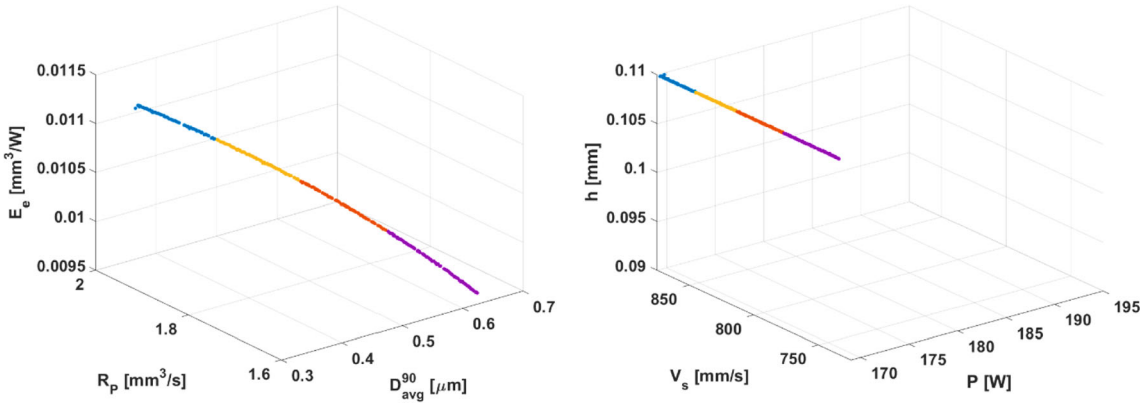

Fig. 33 Multi-objective Genetic Algorithm optimization for maximization of $D_{avg,67}$, R_p, and E_e with objective values (*left*) and the decision variables (*right*)

- Maximize the average grain sizes obtained by the 90° strategy, processing rate, and energy efficiency:

$$\text{Max.}\left\{D_{\text{avg},90}(P, v_s, h), R_p(v_s, h), E_e(P, v_s, h)\right\} \tag{8}$$

- Minimize the average grain sizes obtained by the 90° strategy and maximize processing rate and energy efficiency:

$$\text{Max.}\left\{-D_{\text{avg},90}(P, v_s, h), R_p(v_s, h), E_e(P, v_s, h)\right\} \tag{9}$$

- Maximize the average grain sizes obtained by the 67° strategy, processing rate, and energy efficiency:

$$\text{Max.}\left\{D_{\text{avg},67}(P, v_s, h), R_p(v_s, h), E_e(P, v_s, h)\right\} \tag{10}$$

- Minimize the average grain sizes obtained by the 67° strategy and maximize processing rate and energy efficiency:

$$\text{Max.}\left\{-D_{\text{avg},67}(P, v_s, h), R_p(v_s, h), E_e(P, v_s, h)\right\} \tag{11}$$

- Maximize the magnitude of growth direction angles obtained by 90° strategy, processing rate and energy efficiency:

$$\text{Max.}\left\{\overline{\theta}_{90}(P, v_s, h), R_p(v_s, h), E_e(P, v_s, h)\right\} \tag{12}$$

- Minimize the magnitude of growth direction angles obtained by 90° strategy and maximize processing rate and energy efficiency:

$$\text{Max.}\left\{-\overline{\theta}_{90}(P, v_s, h), R_p(v_s, h), E_e(P, v_s, h)\right\} \tag{13}$$

- Maximize the magnitude of growth direction angles obtained by 67° strategy, processing rate and energy efficiency:

$$\text{Max.}\left\{\overline{\theta}_{67}(P, v_s, h), R_p(v_s, h), E_e(P, v_s, h)\right\} \tag{14}$$

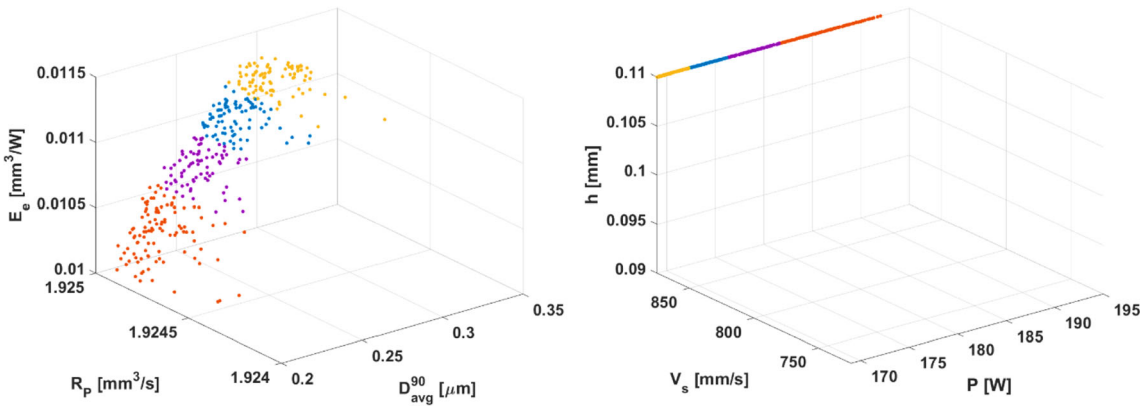

Fig. 34 Multi-objective Genetic Algorithm optimization for minimization of $D_{avg,67}$ and maximization of R_p and E_e with objective values (*left*) and the decision variables (*right*)

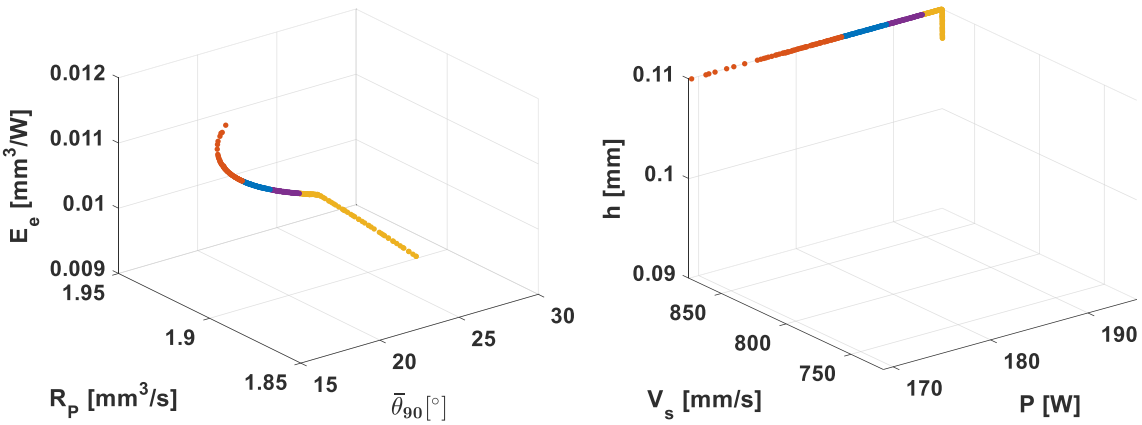

Fig. 35 Multi-objective Genetic Algorithm optimization for maximization of $\bar{\theta}_{90}$, R_p, and E_e with objective values (*left*) and the decision variables (*right*)

- Minimize the magnitude of growth direction angles obtained by 67° strategy and maximize processing rate and energy efficiency:

$$\text{Max.}\left\{-\bar{\theta}_{67}(P, v_s, h), R_p(v_s, h), E_e(P, v_s, h)\right\} \tag{15}$$

For Eqs. (8–15), constraints on the decision variables are defined as follows:

$$\begin{aligned} 169 \le P \le 195 \\ 725 \le v_s \le 875 \\ 0.09 \le h \le 0.11 \end{aligned} \tag{16}$$

Optimizations are run with 200 particles, for 1000 steps or until convergence is reached.

Multi-objective optimization results obtained are shown in Figs. 31, 32, 33, 34, 35, 36, 37, and 38, for the eight different optimization problems defined by Equations 8–15. In each figure, each point represents an optimal solution that forms part of the Pareto front. Also, color sets are utilized in identifying solution sets for each objective function and objective function value for the decision variable set.

Figure 31 shows the solution of the problem described in Eq. 8 where $D_{avg,90}$, R_p, and E_e are maximized. The results show that while E_e and R_p are maximized at high hatch distance and scan velocities with low power, the maximization of $D_{avg,90}$ requires the high power setting. Regions shown in orange and purple provide a good tradeoff between the objectives. Figure 32 shows the solution of the problem described in Eq. 9 where $D_{avg,90}$ is minimized, while maximizing R_p and E_e. Depending on the relative importance of the objectives, process parameters can be chosen accordingly using color regions purple, blue, orange and red.

Fig. 33 shows the solution of the problem described in Eq. 10 where $D_{avg,67}$, R_p, and E_e are maximized (orange colored set). It is seen that the high hatch distance and low power settings are preferred in this case. Lower settings of scan velocity provide larger grain sizes at the cost of processing rate and efficiency. Figure 34 shows the solution of the problem described in Eq. 11 where $D_{avg,67}$ is minimized, while R_p and E_e are maximized (orange color set). High hatch distance and

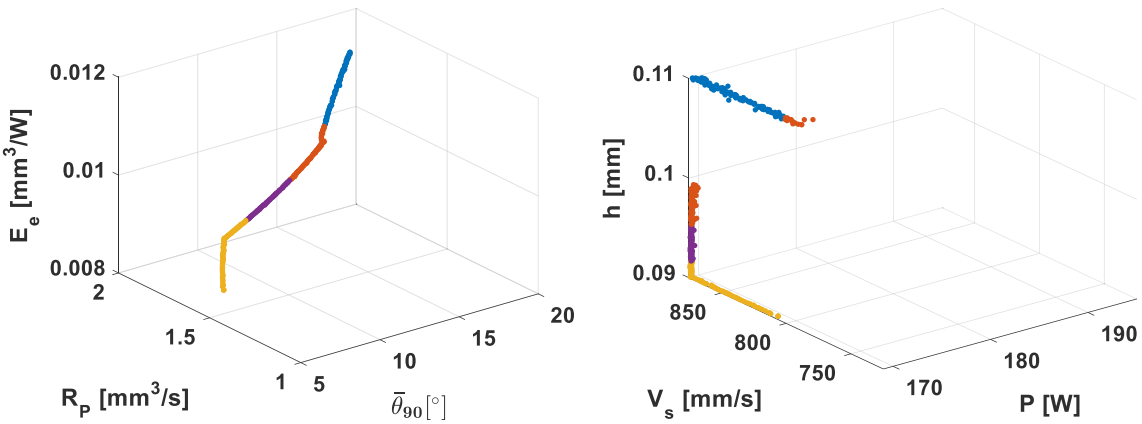

Fig. 36 Multi-objective Genetic Algorithm optimization for minimization of $\bar{\theta}_{90}$ and maximization of R_p and E_e with objective values (*left*) and the decision variables (*right*)

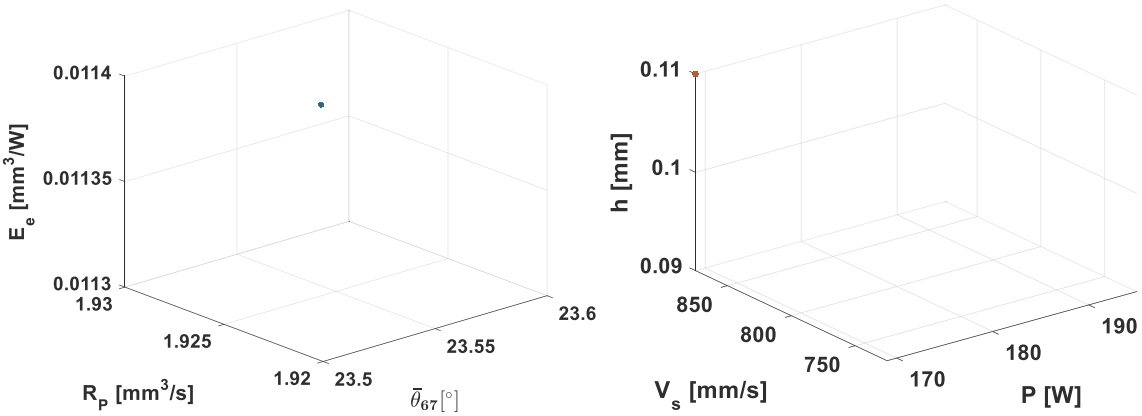

Fig. 37 Multi-objective Genetic Algorithm optimization for maximization of $\bar{\theta}_{67}$, R_p, and E_e with objective values (*left*) and the decision variables (*right*)

scan velocity are preferred in this case, and a tradeoff in the objective function is made with different laser power settings. The processing rate is maximized with high hatch distance and scan velocity settings. High laser power provides smaller grain sizes at the cost of efficiency.

Figure 35 shows the solution of the problem described in Eq. 12 where $\bar{\theta}_{90}$, R_p, and E_e are maximized. In this case, high scan velocity and hatch distance are favored, but the laser power affects the result. Although high laser power seems to maximize the $\bar{\theta}_{90}$ (yellow region), the solution at $h = 0.11$ mm, $v_s = 875$ mm/s, and $P = 169$ W (beginning of orange region) may be preferred. Figure 36 shows the solution of the problem described in Eq. 13 where $\bar{\theta}_{90}$ is minimized, while R_p and E_e are maximized. In this case, low laser power seems to be favored (orange colored set), with variations in hatch distance and scan velocity. If minimization of $\bar{\theta}_{90}$ is the ultimate goal, then the process parameters should be chosen from the yellow region (with $h = 0.09$ mm).

Figure 37 shows the solution of the problem described in Eq. 14 where $\bar{\theta}_{67}$, R_p, and E_e are maximized. Rather than a Pareto front, the solution is converged at a single point, with $P = 169$ W, $v_s = 875$ mm/s, and $h = 0.11$ as these conditions not only maximize the spread between the angles and the z axis but also maximize processing rate and efficiency. Figure 38 shows the solution of the problem described in Eq. 15 where $\bar{\theta}_{67}$ is minimized, while R_p and E_e are maximized (orange colored set). In this case, there is no obvious solution, and a tradeoff must be made. Minimization of $\bar{\theta}_{67}$ is achieved when the process parameters are chosen from the orange region (high laser power, high hatch distance, high velocity). This region also has a relatively high processing rate, at the cost of efficiency.

4 Conclusion

Using laser powder bed fusion (L-PBF), nickel alloy IN625 coupons were built using different laser power, scan velocity, and hatch distance parameters based on a Box-Behnken experiment design. After grinding and electropolishing, SEM images of coupons in XY and XZ faces were taken. Grain sizes on XY surfaces of coupons were measured using a semi-automatic machine-learning classification-based image processing algorithm, and growth directions of columnar

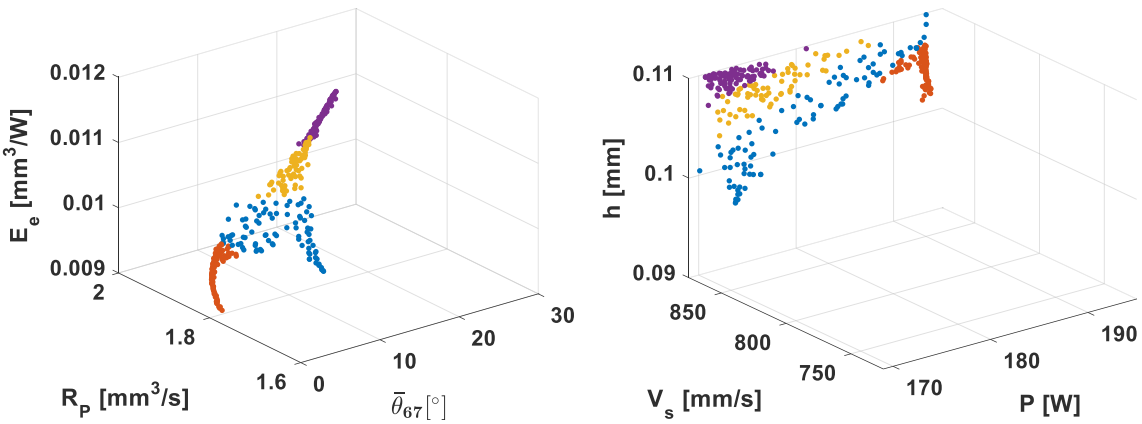

Fig. 38 Multi-objective Genetic Algorithm optimization for minimization of $\bar{\theta}_{67}$ and maximization of R_p and E_e with objective values (*left*) and the decision variables (*right*)

grains with respect to the Z axis were identified on the XZ surfaces using image processing. The results were analyzed using effect plots, and regression models were generated with Response Surface Methodology (RSM). Furthermore, single and multi-objective optimization of microstructural properties as well as processing rate and energy efficiency was performed. Minimization and maximization of grain size and growth directions with different scan strategies were considered in different cases. Process parameters that yield optimum responses with trade-offs were identified. The major finding of this study reveals that the effects of scan strategy and process parameters can be summarized as:

- Increasing energy density results in larger grain sizes; however, the columnar grains tend to grow closer to the build direction with a nonlinear behavior irrespective of scan strategy rotation. However, the growth directions are less influenced by laser power and scan velocity when a scan strategy rotation of 67°is used.
- Finer grain sizes can be obtained when process parameters optimized using a scan strategy rotation of 67°.
- A combination of medium-high scan velocity and medium hatch distance is seen as ideal for growth aligning in the build direction and resulting in an isotropic build.

Acknowledgments This project was supported by the National Institute of Standards and Technology, United States Department of Commerce, under the financial assistance number 70NANB14H227.

References

1. Amato KN, Gaytan SM, Murr LE, Martinez E, Shindo PW, Hernandez J, Collins S, Medina F (2012) Microstructures and mechanical behavior of Inconel 718 fabricated by selective laser melting. Acta Mater 60:2229–2239
2. Anam MA, Dilip JJS, Pal D, Stucker B (2014) Effect of scan pattern on the microstructural evolution of Inconel 625 during selective laser melting. Proceedings of 25th Annual International Solid Freeform Fabrication Symposium, August 4–6, 2014, Austin, Texas
3. Brinksmeier E, Levy G, Meyer D, Spierings AB (2010) Surface integrity of selective-laser-melted components. CIRP Ann Manuf Technol 59(1):601–606
4. Carter LN, Martin C, Withers PJ, Attallah MM (2014) The influence of the laser scan strategy on grain structure and cracking behaviour in SLM powder-bed fabricated nickel super alloy. J Alloys Compd 615:338–347
5. Criales L, Arisoy YM, Özel T (2016) Sensitivity analysis of material and process parameters in finite element modeling of selective laser melting of Inconel 625. Int J Adv Manuf Technol In press
6. Deb K (2001) Multi-objective optimization using evolutionary algorithms. John Wiley & Sons, Inc
7. Hernandez J, Murr LE, Amato KN, Martinez E, Shindo PW, Terrazas CA, Rodriguez E, Medina F, Wicker RB, Li SJ, Cheng XY, Yang F (2012) Microstructures and properties for a superalloy powder mixture processed by electron beam melting. J Materials Science Research 1:124–144
8. Hong C, Gu D, Dai D, Alkhayat M, Urban W, Yuan P, Cao S, Gasser A, Weisheit A, Kelbassa I, Zhong M, Poprawe R (2015) Laser additive manufacturing of ultrafine TiC particle reinforced Inconel 625 based composite parts: tailored microstructures and enhanced performance. Mater Sci Eng A 635:118–128
9. Jia Q, Gu D (2014) Selective laser melting additive manufacturing of Inconel 718 superalloy parts: densification, microstructure and properties. J Alloys Compd 585:713–721
10. Khairallah SA, Anderson AT, Rubenchik A, King WE (2016) Laser powder-bed fusion additive manufacturing: physics of complex melt flow and formation mechanisms of pores, spatter, and denudation zones. Acta Mater 108:36–45
11. Krauss H, Zeugner T, Zaeh MF (2014) Layerwise monitoring of the selective laser melting process by thermography. Phys Procedia 56: 64–71
12. Kruth JP, Levy G, Klocke F, Childs THC (2007) Consolidation phenomena in laser and powder-bed based layered manufacturing. CIRP Ann- Manuf Technol 56(2):730–759
13. Lawrence JR, Pou J, Low DK, Toyserkani E (2010) Advances in laser materials processing: technology, research and application. Elsevier
14. Li S, Wei Q, Shi Y, Zhu Z, Zhang D (2015) Microstructure characteristics of Inconel 625 superalloy manufactured by selective laser melting. J Mater Sci Technol 31(9):946–952
15. Liu F, Lin X, Huang C, Song M, Yang G, Chen J, Huang W (2011) The effect of laser scanning path on microstructures and mechanical properties of laser solid formed nickel-base superalloy Inconel 718. J Alloys Compd 509:4505–4509
16. Mercelis P, Kruth JP (2006) Residual stresses in selective laser sintering and selective laser melting. Rapid Prototyp J 12(5):254–265
17. Mitchell M (1996) An introduction to genetic algorithms. MIT Press
18. Murr LE, Gaytan SM, Ramirez DA, Martinez E, Hernandez J, Amato KN, Shindo PW, Medina FR, Wicker RB (2012a) Metal fabrication by additive manufacturing using laser and electron beam melting technologies. J Mater Sci Technol 28:1–14
19. Murr LE, Martinez E, Amato KN, Gaytan SM, Hernandez J, Ramirez DA, Shindo PW, Medina F, Wicker RB (2012b) Fabrication of metal and alloy components by additive manufacturing: examples of 3D materials science. J Mater Res Technol 1:42–54
20. Ramos JA, Murphy J, Lappo K, Wood K, Bourell DL, Beaman JJ (2002) Single-layer deposits of nickel base superalloy by means of selective laser melting. Proceedings of 13th Solid Freeform Fabrication Symposium, August 5–7, 2002, Austin, Texas
21. Thepsonthi T, Özel T (2012) Multi-objective process optimization for micro-end milling of Ti-6Al-4V titanium alloy. Int J Adv Manuf Technol 63:903–914
22. Ulutan D, Özel T (2013) Multi-objective optimization of experimental and simulated residual stresses in turning of nickel-alloy IN100. Mater Manuf Process 28:835–841
23. Vilaro T, Colin C, Bartout JD, Nazé L, Sennour M (2012) Microstructural and mechanical approaches of the selective laser melting process applied to a nickel-base superalloy. Mater Sci Eng A 534:446–451
24. Wang Z, Guan K, Gao M, Li X, Chen X, Zeng X (2012) The microstructure and mechanical properties of deposited IN718 by selective laser melting. J Alloys Compd 513:518–523